IMAGE STABILIZATION PERFORMANCE OPTIMIZATION USING AN OPTICAL REFERENCE GYROSCOPE

JEFFEREY T. HAMMANN

B.S., Aerospace Engineering, University of Colorado
Boulder, Colorado (1986)

Submitted to the Department of Aeronautics and Astronautics
in Partial Fulfillment of the Requirements for the Degree of

MASTER OF SCIENCE in AERONAUTICS AND ASTRONAUTICS

at the

MASSACHUSETTS INSTITUTE OF TECHNOLOGY

June 1992

Signature of Author _____
Department of Aeronautics and Astronautics
May 8, 1992

Approved by _____
Dr. Tze-Thong Chien
Principal Member Technical Staff, Charles Stark Draper Laboratory
Technical Supervisor

Certified by _____
Dr. Harold L. Alexander
Bradley Career Development Assistant Professor,
Department of Aeronautics and Astronautics
Thesis Advisor

Accepted by _____
Prof. Harold Y. Wachman
Chairman, Department Graduate Committee

IMAGE STABILIZATION PERFORMANCE OPTIMIZATION

USING AN OPTICAL REFERENCE GYROSCOPE

by

JEFFEREY T. HAMMANN

Submitted to the Department of Aeronautics and Astronautics on May 8, 1992 in partial fulfillment of the requirements for the Degree of Master of Science in Aeronautics and Astronautics.

Abstract

An optical reference gyroscope (ORG) provides an inertially stabilized collimated optical reference beam, which, in conjunction with a fast steering mirror (FSM), allows for closed-loop control image stabilization. Feedback-control permits attenuation in the image space of base motion disturbances which would tend to distort and shift the image at the focal plane. Transfer function derivations for the components and system yield the detector and image error equations. A numerical parametric study of the compensator design seeks to minimize the image error, taking into account ORG noise, base motion power spectra and ORG base-to-rotor coupling effects. A Fourier spectrum analysis of the remaining image error helps to predict the contributions to scene shift and distortion at the focal plane and the resulting image quality degradation at the charge-coupled-device imager. Analytical results are compared with test results.

Technical Supervisor: Dr. Tze-Thong Chien
Principal Member Technical Staff,
Charles Stark Draper Laboratory

Thesis Supervisor: Dr. Harold L. Alexander
Bradley Career Development Assistant
Professor, Department of Aeronautics and
Astronautics

Acknowledgements

My sincerest gratitude is extended to my thesis supervisor, Dr. T.T. Chien, for his patience and assistance in helping me keep my focus in my education and on this research. His keen insights into matters, technical or otherwise, were invaluable.

I also extend my gratitude to my thesis advisor, Professor "Sandy" Alexander, for his interest and unwavering support of my efforts.

This educational experience would not have been quite as complete if I had not had the pleasure of experiencing the "real world" of engineering testing by working side-by-side with Dale Woodbury; the quintessential "master test pilot" of new and unique guidance systems.

Special thanks are given to Mike Luniewicz, Linda Fava, Linda Willy, Greg Capiello and Steve Christensen for listening to my naive questions and helping to educate me in their fields of expertise. Special thanks are also given to Joan, John and Loretta of the Draper Education Office and Liz Zotos of the MIT Aero/Astro office for their very professional administrative support and interest in my endeavors.

I cannot go without expressing very special thanks to two individuals who helped to round out the New England experience for me: to Angie Emberley for taking me under her kind-hearted wing and making me feel at home and to Stephen Helfant for spending his time and enthusiasm introducing me to a fascinating hobby.

To all the others who have helped me: thank you!

This thesis was researched and written at the Charles Stark Draper Laboratory under Internal Research & Development (IR&D) project #328.

Publication of this thesis does not constitute approval by the laboratory of the findings or conclusions herein, but is done for the exchange and stimulation of ideas.

Table of Contents

List of Figures

List of Acronyms

ACTS	Advanced Communications Technology Satellite
ADS	Angular Displacement Sensor
CCD	Charge Coupled Device
CSDL	Charles Stark Draper Laboratory
DYNAC	Dynamic Autocollimator
FSM	Fast Steering Mirror
IRU	Inertial Reference Unit
LED	Light emitting diode
LITE	Laser Intersatellite Tracking Experiment
LOS	Line Of Sight
ORG	Optical Reference Gyroscope
PID	Proportional-Integral-Derivative
PSD	Power Spectral Density
RMS	Root Mean Square

1 Introduction

1.1 Background

Images taken from focal plane assemblies mounted on aircraft or spacecraft suffer image degradation due to platform disturbances. Depending upon the specific application, the amount of image degradation due to these disturbances may either be acceptable or require stabilization during imaging and/or post-processing.

One method used to reduce image degradation is to apply tight pointing control on the platform so that the peak or RMS angular disturbances contribute only an acceptable level to the image error budget. A prime example of this technique is on the Hubble Space Telescope (HST) where attitude pointing requirements of .007 arc second were imposed in order to get the specified optical resolution [1]. It employs closed-loop control on the platform using rate gyros and a precision star tracker for sensing attitude and reaction wheels damped by magnetic torque bars for applying control torques.

Post-processing techniques may also be used on a digitized image in conjunction with or in lieu of platform control. These techniques may be classified as image restoration or image enhancement [2]. Image restoration requires some knowledge of the disturbance spectra during the image integration period which can then be used with computational deconvolution (or other) processes to restore some of the image quality. Deconvolution techniques have been used on images from the HST to remove the "spider-like" distortions caused by the primary mirror's incorrect curvature. Image enhancement involves operating on the image data point spread functions, without any record of the disturbance sources, to increase contrast, suppress noise or to manipulate the data so that only specified features of interest are enhanced and all others subdued. Image enhancement should be performed after image restoration for maximum improvement of image quality by post-processing techniques.

For the best possible image quality, the image at the focal plane should be as free from platform-induced distortion as possible. In some instances this is accomplished by controlling the platform, which for large, high inertia systems, may be quite difficult for other than a very low bandwidth. The next logical step is to stabilize the optical path on the platform. The optical elements involved are typically very low inertia actuators, such as fast steering mirrors that are capable of very high bandwidths (1 KHz).

There are numerous examples of systems using optical path stabilization. One of these is the STARLAB experiment [3], which is a shuttle on-orbit demonstration program of acquisition, laser tracking and pointing techniques critical to the strategic defense directed energy concepts. It uses an inertial angle sensor whose output is fed forward to a fast steering mirror to reject base motion disturbances so that a laser diode's output is stabilized on a vibration sensor. The Zenith Star experiment [4] (a part of the strategic defense directed energy concepts program) also uses a fast steering mirror for correcting laser beam jitter and fine pointing. In this system, an alignment reference platform uses an inertial reference unit to provide attitude information which is fed forward to provide open loop disturbance rejection. Although these two systems are not imaging systems, the problems are similar in that the goal for both types is a stabilized optical path from a source to a "receiver". In these cases the source is a laser, which is collimated, expanded and directed to a target and in the imaging system the energy is received from the target, compressed and sent to a "receiver" (e.g. a charge-coupled device (CCD)). The primary optical paths are very similar.

As already noted, the two systems mentioned above (in addition to all other systems with similar purpose) use inertial reference units (IRUs) which feed forward attitude information for disturbance rejection. Such open loop control methods are subject to scale factor errors of the IRUs and the fast steering mirrors. In addition, since no real system is perfectly rigid, there may be modal disturbances in the optical path between the platform optical elements due to

platform jitter. For a system with extremely tight pointing requirements, these error sources may exceed specification at the focal plane. Closed-loop control techniques would minimize the sensitivity of the disturbance rejection system to the error sources noted above. Compensating for platform effects requires an inertial reference beam that follows the same optical path as the target image on the platform. Nulling the reference beam detector error with closed-loop control of a fast steering mirror in the common optical paths then simultaneously stabilizes the target on the focal plane.

It is for this purpose that the optical reference gyro (ORG) was developed by Charles Stark Draper Laboratory [5,6]. The ORG is a 2-axis dry-tuned gyro providing a stabilized, collimated beam. A pinhole, illuminated by a laser source, diffracts the light into a collimating lens which is mounted on an inertially stabilized spinning rotor, with the lens focal point located at the pinhole.

This thesis examines the performance of an experimental closed-loop optical disturbance rejection system incorporating the ORG.

1.2 System Description

In this Draper Laboratory research and development project all the system elements are mounted on a common base which may be perturbed to simulate platform disturbances (see figure 1.2-1).

The ORG provides an inertial reference--a pseudo star. It is a dry-tuned, 2-axis gyroscope which allows the reference beam to remain inertially fixed even though platform jitter is coupled to the ORG case. The emerging reference beam is sent through an extended corner-cube retroreflector so that it follows the same optical path as the target image, passing through a beam compressor onto a high bandwidth fast steering mirror (FSM).

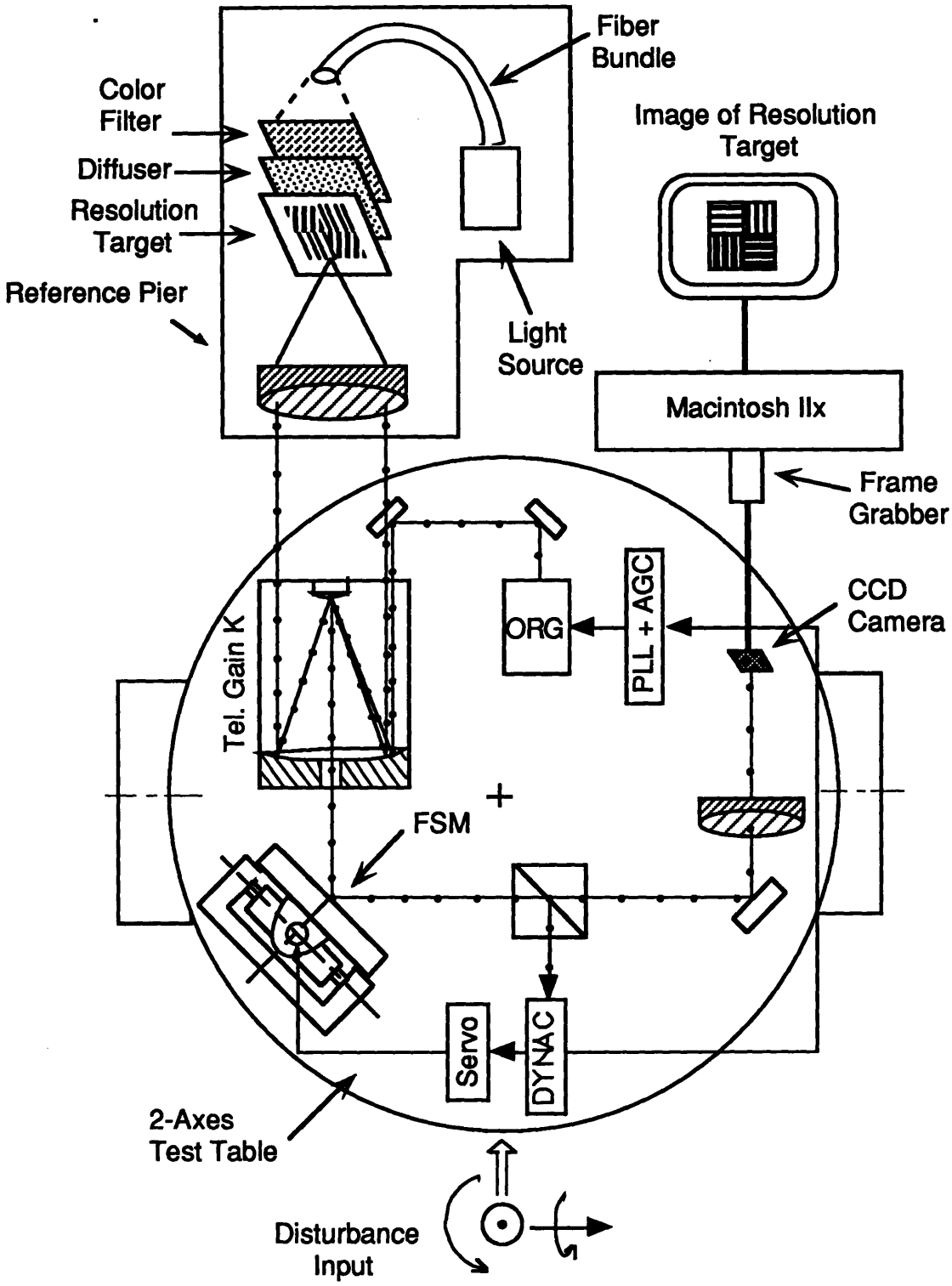

Figure 1.2-1. Image stabilization configuration.

The FSM deflects the composite image through a nominal 90 degrees onto a dichroic beam splitter, which passes wavelengths shorter than 700 μm and reflects longer wavelengths. The target scene passes through the beam splitter undeflected and onto a fixed mirror, into a focusing lens system and onto a CCD camera for recording. The reference beam is reflected nominally by 90 degrees onto a quadrant photodetector which is used to detect angular deflections on 2 axes with respect to a base fixed frame. This error is fed back to a servomechanism for controlling the FSM to compensate optically for base motion disturbances.

1.3 Thesis Goals

The primary goal of this thesis is to systematically analyze the imaging system described herein and to design a compensator for it which provides the best possible trade-off between disturbance rejection and sensor noise. This requires modeling the system, derivating its transfer functions, characterizing system inputs, parameterizing the compensator, analyzing system outputs as a function of the compensator parameter, investigation of possible system modifications to improve performance, and comparing analysis results with actual test data. In addition, the output spectrum is analyzed in an attempt to discriminate between image shift and smear (distortion) and their contributions to image quality degradation.

1.4 Thesis Roadmap

The system components are first described in detail before identifying assumptions and simplifications. The element and system block diagrams are shown and the transfer functions are then derived, identifying the system inputs. Next, the input power spectral densities (PSDs) are quantified. The analytical study identifies the compensator type selection rationale, paramaterization, and the optimization analysis methodology. The output power spectrum is then treated statistically using Fourier methods to

separate the image error into image shift and distortion, which are then considered as to what they contribute to image degradation. The analysis results are then compared with test results to validate the modeling and analysis methodology before summarizing the study results and making recommendations for areas of further research.

2 System Component Descriptions

2.1 Optical Reference Gyroscope

The ORG is a two degree-of-freedom, dry tuned flexure suspended gyro. See figure 2.1-1 for a cross-sectional view of the ORG and reference 1 for a more detailed description of the ORG. It consists of a .7 inch aperture achromatic collimating lens assembly mounted on the forward end of a rotor and an 8 micron pinhole on the aft end. The rotor is mounted on a motor shaft by a two-axis flexure hinge. The motor shaft is supported by twin ball bearing sets on the aft end and is spun by a brushless permanent magnet. The rotor may be commanded to move (orthogonal to the spin axis) within the case by a torque motor. Case-to-rotor rotational isolation is provided by the flexure hinge which consists of two concentric cylindrical hinges, each of which has two diagonal cuts which stop short of each other, leaving a small thickness of material on each side which act as flexure springs. The two cylinders are glued together with their hinges at right angles. Inductive pickoffs provide case-to-rotor angles. The rotor spin frequency is tuned to 89.4 Hz so that the dynamic gyro stiffness exactly cancels out the hinge spring forces, providing zero net torque on the rotor. Thus, even if the case rotates through a small angle, the rotor will remain inertially fixed.

A laser beam, generated by a laser diode and conducted via an optical fiber, is collimated and then converged to a focus just short of the pinhole by a lens assembly on the aft end of the ORG rotor so that it uniformly illuminates the region of the pinhole. The diffraction pattern diverging from the pinhole is collimated by the lenses at the forward end of the rotor, which produces an inertially stabilized central Airy disk on the order of 10 mm in diameter. Perfect alignment of the pinhole, the optical axis and the rotor spin axis was not possible, and therefore noise at the spin speed exists in the ORG reference beam. Indeed, initially more than 90% of the ORG noise power was at the spin speed.

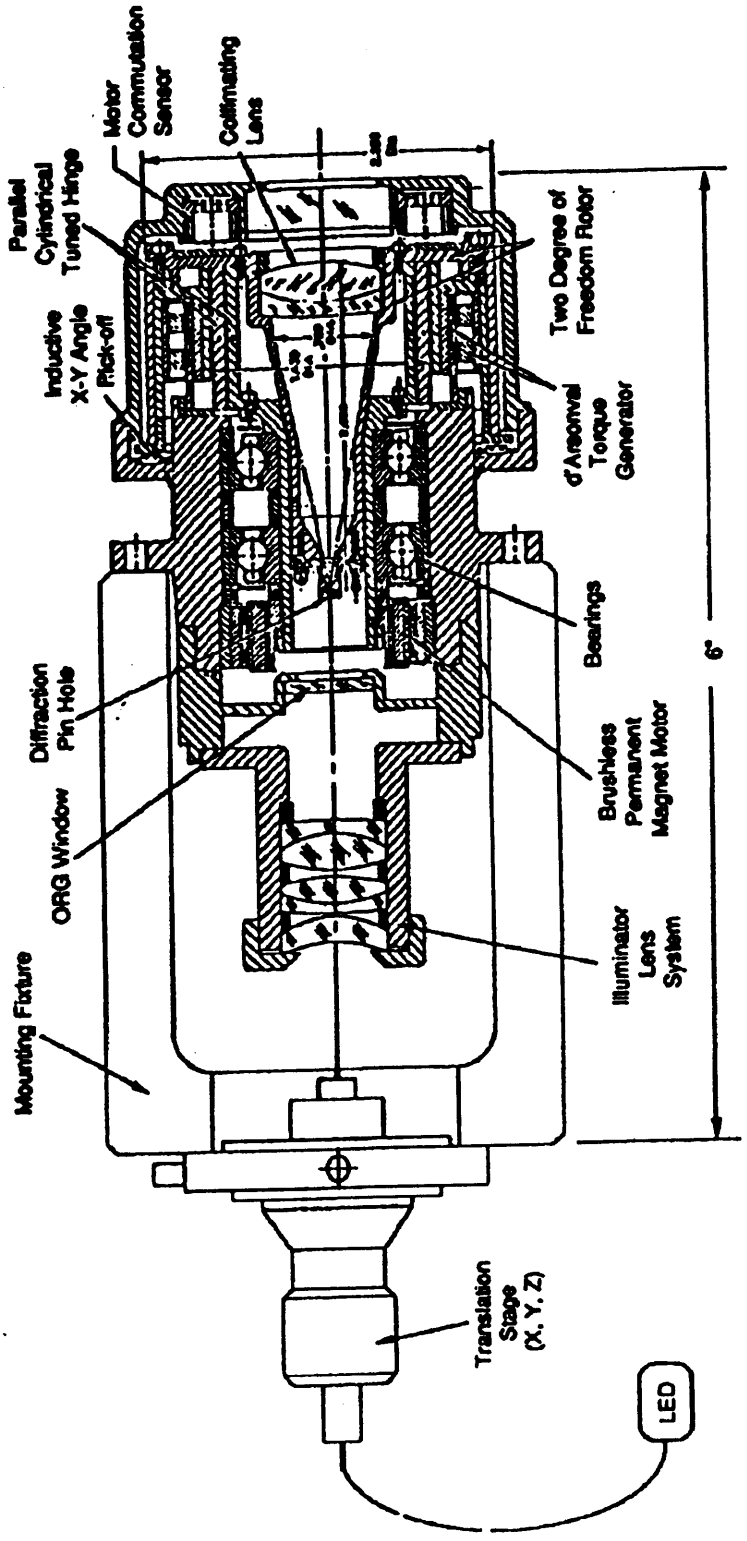

Figure 2.1-1. ORG cross-sectional view.

A unique noise compensator, referred to as a Subtraction Eliminator, with a notch bandwidth of several Hertz was designed and incorporated into the system to eliminate the spin frequency noise component [5]. This device can either electronically eliminate the noise at the output of an optical detector or it can be used to mechanically eliminate the noise by providing a torquing signal to the ORG. The reference beam also has a large noise component at the rotor nutation frequency of 133 Hz and lesser noise components at harmonics of the spin speed. Wideband components of the noise power are probably primarily due to illumination source variations. The ORG has been evacuated to <10 microns Hg to reduce the noise floor and case-to-rotor coupling resulting from gas dynamics.

2.2 Fast Steering Mirror

The fast steering mirror (FSM) was designed and built by Hughes Aircraft Company. Since much of the FSM technical detail is proprietary, only general design specifications or measured performance figures are presented.

The FSM consists of a very low inertia 5" diameter mirror with a measured RMS surface roughness of approximately $\lambda/10$ using a helium-neon laser. Four permanent magnet voice coil actuators drive the lightweight mirror with a maximum peak acceleration of 1000 rad/sec^2. The mirror is mounted on proprietary Hughes Aircraft Company cross-blade flexures. The system is a reactionless design and has low resistance in the pivot axes with a very high cross-axis compliance, assuring a constant center-of-rotation location over the entire range of travel. KAMAN proximity sensors provide extremely high accuracy over limited mirror travel for internal position control. The FSM comes equipped with an adjustable analog servomechanism compensation module and separate paths for internal and external feedback control.

2.3 Optical Detector

The optical detector for this system is a DYNAC [6], which is an acronym for dynamic autocollimator. Figure 2.3-1 shows a simplified diagram of a single axis DYNAC. It consists of a lens which focuses the incoming beam onto a bi-lens that divides the light between two photocells.

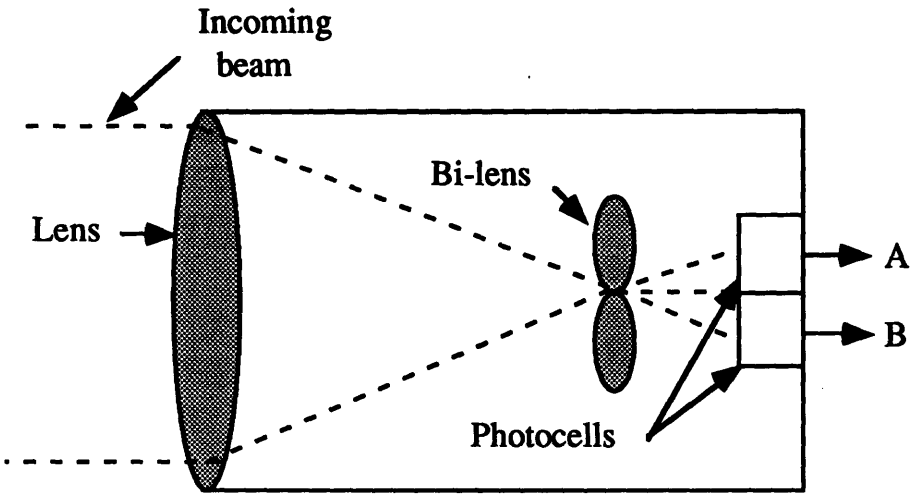

Figure 2.3-1. Simplified diagram of a single axis DYNAC.

If the input beam angle changes, then the percentage of light going to the two photocells also changes. If one of the photocell outputs is called A and the other B, then the input angle θ is proportional to A-B. To reduce errors due to intensity fluctuations, the difference is normalized by the sum, with K being a proportionality constant:

$$\theta = K \frac{A-B}{A+B}$$

For this experiment it is necessary to measure rotations about two axes, and therefore a dual-axis DYNAC is used which has a quad-lens configuration and four photocells but is, in principle, exactly the same as that described above. The DYNACs are extremely quiet devices, with a typical noise measurement of approximately 20 nanoradians RMS from .1 to100 Hz.

2.4 Imaging Sensor

The imaging sensor consists of several elements, including:

1. Beam compressor
2. Focusing lens set
3. Pulnix TM-7CN CCD camera
4. RasterOps 364 frame grabber
5. Macintosh IIx computer

The beam compressor is a Cassegranian type with a parabolic primary mirror and a hyperbolic secondary providing a collimated output beam whose diameter is reduced (relative to the primary's diameter) by the compressor gain factor k. The beam compressor used in this analysis has a gain factor of 4.

The image must remain in the collimated state for transit along the platform optical path so that changes in the path length do not affect the focus. After the last reflecting element in the optical path, a focusing lens assembly provides the required convergence of the beam for proper focus of the image on the CCD focal plane.

The Pulnix CCD camera provides a variable shutter speed of from 1/30th second to 1/10,000th second.

3 System Modeling

3.1 Assumptions

The following are the major assumptions used in the analysis:

1. The target is fixed in inertial space, thus tracking is not analyzed in this thesis. Both the ORG and FSM, however, can be commanded for target tracking.

2. The ORG noise and base motion power spectra are uncorrelated, stochastic processes. It will be shown later that there is case-to-rotor coupling within the ORG which can be represented as a modification of the base motion-to-error transfer function.

3. The mirror dynamics can be represented a linear, second order system. The actual measured non-linearity is .27% full scale.

4. The two mirror axes are dynamically decoupled. Measured data show cross-coupling between axes is 1.58% or -37 dB.

5. The optical detector noise is negligible. The actual detector noise is 20 nanoradians RMS from .1 to100 Hz.

6. The platform and beam compressor exhibit only rigid body modes. Though the flexible mode effects are not analyzed herein, since both the target LOS and the reference beam follow the same optical path through the beam compressor on the platform, the system should theoretically compensate for them as common mode errors.

3.2 Geometry Analysis

In order to derive the error transfer functions, the quantitative effect of 2-axis mirror rotations with respect to the reference line-of-sight (LOS) must be examined. This is done by first assuming that

the beam incident on the mirror is fixed in inertial space (i.e. no platform disturbances or ORG noise).

The base/mirror geometry is illustrated in figure 3.2-1. The base fixed frame is the x_b, y_b, z_b set where y_b and z_b are the respective directions of the incident and reflected beams with no base or mirror rotations, and thus z_b is the camera LOS to be stabilized. The x_m, y_m, z_m set is fixed in the base frame with x_m and y_m being the fixed mirror rotation axes and the z_m axis is the non-rotated mirror normal. The x'_m, y'_m, z'_m set is the mirror fixed frame which rotates with the mirror. R' is the actual reflected beam direction which must be found to calculate the angle it makes with z_b in the y_b, z_b plane (azimuth) and the angle it makes normal to the y_b, z_b plane (elevation). The incidence angle ϕ_i is nominally $\pi/4$ radians.

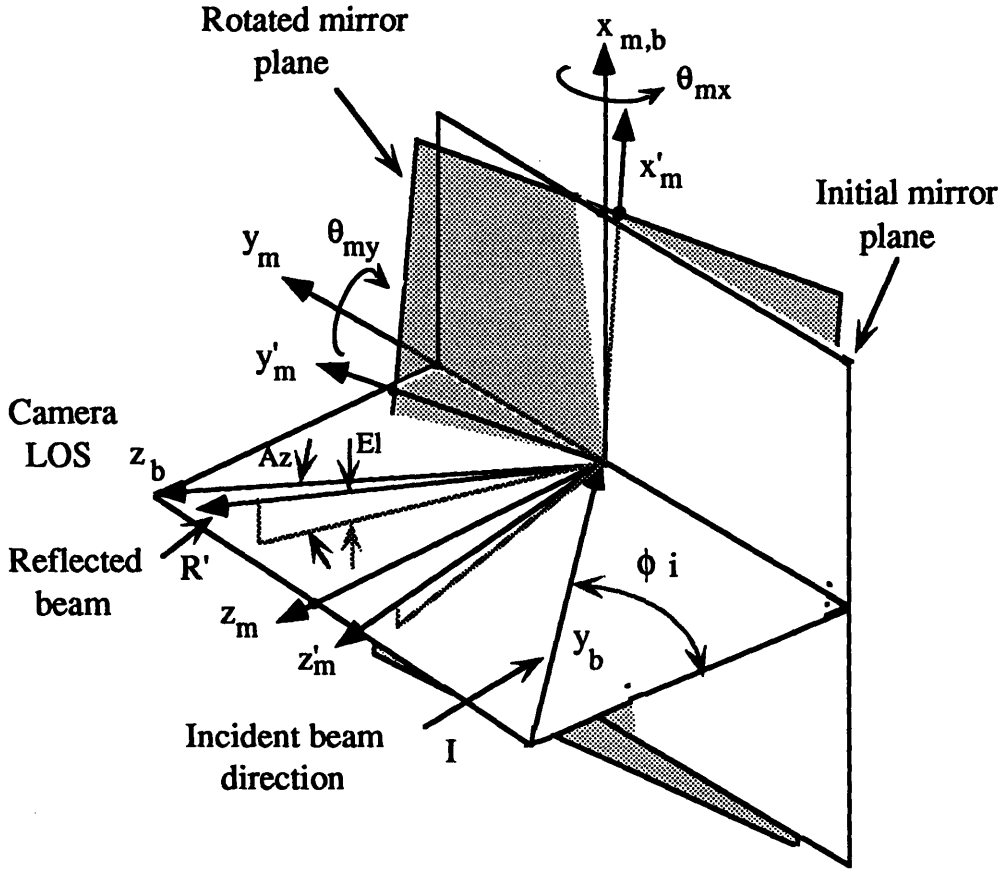

Figure 3.2-1 Base fixed and mirror coordinate frames.

Note that a pure rotation about just the y_m axis will result in a change in elevation with the same sign and a second order change in azimuth, always negative. This can be most easily visualized as θ_{my} approaches a limiting value of $\pi/2$ radians. In the limit, the incident beam would not be reflected, therefore the azimuth change would be $-\pi/2$ radians and the elevation change would be π radians. Also, a rotation about the x axis will affect the sensitivity ($\Delta Az/\Delta \theta_{my}$) to y-axis rotations, which is proportional to $\cos\phi$.

To calculate azimuth and elevation changes, the incident beam direction is transformed from the base frame to the rotated mirror frame, from which the reflected beam is derived by changing the sign of the normal component. Using the inverse transformation to take the reflected beam into base fixed coordinates then allows the azimuth and elevation errors to be calculated from the reference directions.

The transformation from the base frame to the non-rotated mirror frame, for an arbitrary vector, is given by:

$$\begin{pmatrix} x \\ y \\ n \end{pmatrix}_m = \begin{bmatrix} 1 & 0 & 0 \\ 0 & \sin\phi & \cos\phi \\ 0 & -\cos\phi & \sin\phi \end{bmatrix} \begin{pmatrix} x \\ y \\ z \end{pmatrix}_b \qquad (3.2\text{-}1)$$

The transformation from the reference mirror frame to the rotated frame is then given by:

$$\begin{pmatrix} x \\ y \\ n \end{pmatrix}_{m'} = \begin{bmatrix} \cos\theta_{my} & 0 & -\sin\theta_{my} \\ \sin\theta_{mx}\sin\theta_{my} & \cos\theta_{mx} & \sin\theta_{mx}\cos\theta_{my} \\ \cos\theta_{mx}\sin\theta_{my} & -\sin\theta_{mx} & \cos\theta_{mx}\cos\theta_{my} \end{bmatrix} \begin{pmatrix} x \\ y \\ n \end{pmatrix}_m \qquad (3.2\text{-}2)$$

If we now assume that the rotations are small (<< 1 deg), then the last transformation can be approximated by:

$$\begin{pmatrix} x \\ y \\ n \end{pmatrix}_{m'} \approx \begin{bmatrix} 1 & 0 & -\theta_{m\,y} \\ 0 & 1 & \theta_{m\,x} \\ -\theta_{m\,x} & 1 & \end{bmatrix} \begin{pmatrix} x \\ y \\ n \end{pmatrix}_{m} \qquad (3.2\text{-}3)$$

Then the transformation from the base frame to the rotated mirror frame is given, after inserting equation 3.2-1 into 3.2-3, by:

$$\begin{pmatrix} x \\ y \\ n \end{pmatrix}_{m'} = \begin{bmatrix} 1 & \theta_{my}\cos\phi & -\theta_{my}\sin\phi \\ 0 & \sin\phi-\theta_{mx}\cos\phi & \cos\phi+\theta_{mx}\sin\phi \\ \theta_{my} & -\cos\phi-\theta_{mx}\sin\phi & \sin\phi-\theta_{mx}\cos\phi \end{bmatrix} \begin{pmatrix} x \\ y \\ z \end{pmatrix}_{b} \qquad (3.2\text{-}4)$$

Now, the incidence beam (I) direction in the base frame is just y_b (i.e: $[0, 1, 0]^T$). Inserting this vector into equation 3.2-4 gives I in the rotated mirror frame :

$$I_{m'} = \begin{pmatrix} \theta_{my}\cos\phi \\ \sin\phi-\theta_{mx}\cos\phi \\ -\cos\phi-\theta_{mx}\sin\phi \end{pmatrix} \qquad (3.2\text{-}5)$$

The reflected beam (R') is just the incident beam but with the negative of the normal (z) component, so the reflected beam in the rotated mirror frame is:

$$R'_{m'} = \begin{pmatrix} \theta_{my}\cos\phi \\ \sin\phi-\theta_{mx}\cos\phi \\ \cos\phi+\theta_{mx}\sin\phi \end{pmatrix} \qquad (3.2\text{-}6)$$

Transforming the reflected beam back to the base frame just requires multiplying the transpose (inverse) of the b-to-m' transformation matrix in equation 3.2-4 by the reflected vector given above to give:

$$R_b = \begin{pmatrix} \theta_{my}\cos\phi(2-\theta_{mx}^2)+2\theta_{mx}\theta_{my}\sin\phi \\ 1-2\cos^2\phi-2\theta_{mx}\sin 2\phi+(\theta_{mx}^2+\theta_{my}^2)\cos^2\phi-\theta_{mx}^2\sin^2\phi \\ \sin 2\phi+2\theta_{mx}(\sin^2\phi-\cos^2\phi)-\sin 2\phi(2\theta_{mx}^2+\theta_{my}^2) \end{pmatrix} \qquad (3.2\text{-}7)$$

Dropping other than first-order terms and using the trigonometric identity

$$\sin^2\phi-\cos^2\phi \;=\; 1-2\cos^2\phi$$

gives:

$$R_b \approx \begin{pmatrix} 2\theta_{my}\cos\phi \\ 1-2\cos^2\phi-2\theta_{mx}\sin 2\phi \\ \sin 2\phi+2\theta_{mx}(1-2\cos^2\phi) \end{pmatrix} \qquad (3.2\text{-}8)$$

For a nominal incidence angle of 45 degrees in the base frame, the reflected beam is given by:

$$R_b \approx \begin{pmatrix} \sqrt{2}\theta_{my} \\ -2\theta_{mx} \\ 1 \end{pmatrix} \qquad (3.2\text{-}9)$$

We can now compute the azimuth and elevation errors from the camera LOS by examining figure 3.2-1. The azimuth error is found to be, to first order, assuming small rotations:

$$Az = \tan^{-1}\left(\frac{-R_{by}}{R_{bz}}\right) = \tan^{-1}\left(\frac{2\theta_{mx}}{1}\right) \approx 2\theta_{mx} \qquad (3.2\text{-}10)$$

The minus sign in the first ratio arises from the fact that a negative change in the y component corresponds to a positive rotation about the x axis. The elevation error is similarly calculated as:

$$El = \tan^{-1}\left(\frac{R_{bx}}{\sqrt{R_{by}^2+R_{bz}^2}}\right) = \tan^{-1}\left(\frac{\sqrt{2}\theta_{my}}{\sqrt{1+4\theta_{mx}^2}}\right) \approx \sqrt{2}\theta_{my} \qquad (3.2\text{-}11)$$

This analysis reveals that the error contributions due to geometric coupling between the axes are of second order or smaller magnitude and may, therefore, be ignored for analysis purposes for small rotations. This fact, in conjunction with the weak mirror dynamical cross-coupling, allows analytical treatment of the compensator design as two separate, simpler single output problems rather than a multiple-input, multiple-output problem.

Incident beam deviations from the base-fixed y axis could have been included in this analysis to show their effect, but they would have tended to complicate the results and their effects are easily seen: a positive x or z rotation of the incident beam produces an equal but negative azimuth or elevation error, respectively.

Now that the geometrical effects have been quantified, the mirror dynamics will be examined before looking at the entire system.

3.3 Fast Steering Mirror

Figure 3.3-1 is a block diagram of a single mirror axis dynamics where:

θ_b^i : base motion with respect to inertial frame
θ_m^i : mirror rotation with respect to inertial frame
U : control signal input to mirror

Both axes have the same representation.

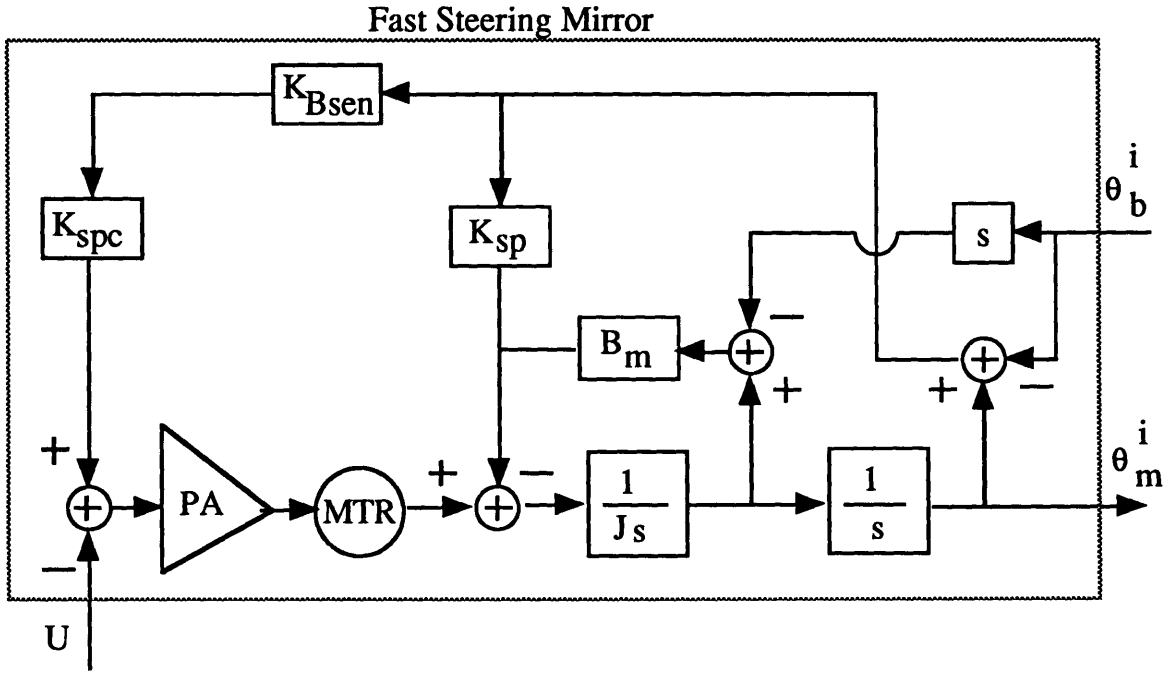

Figure 3.3-1. FSM block diagram for a single axis.

From the diagram above it can be shown that

$$\theta_m^i = \frac{1}{Js^2}\left(K_{sp}(\theta_b^i-\theta_m^i)+sB_m(\theta_b^i-\theta_m^i)-PA*MTR(K_{Bsen}K_{spc}(\theta_b^i-\theta_m^i)+U)\right)$$

(3.3-1)

We would like to get equation (3.3-1) in the form $\theta_m^i = F(B\,\theta_b^i - U)$ so that it can be represented as in figure 3.3-2.

Let PA*MTR = P and let $K_{eq} = K_{sp} - PK_{Bsen}K_{spc}$.

Then solving for θ_m^i gives :

$$\theta_m^i = \frac{(B_m s + K_{eq})\theta_b^i - P*U}{\Delta} \qquad (3.3\text{-}2)$$

where $$\Delta = Js^2 + B_m s + K_{eq}. \qquad (3.3\text{-}3)$$

So $$F(s) = \frac{P}{\Delta} \qquad (3.3\text{-}4)$$

and $$B(s) = \frac{(B_m s + K_{eq})}{P} \qquad (3.3\text{-}5)$$

The mirror dynamics can now be represented by the block diagram:

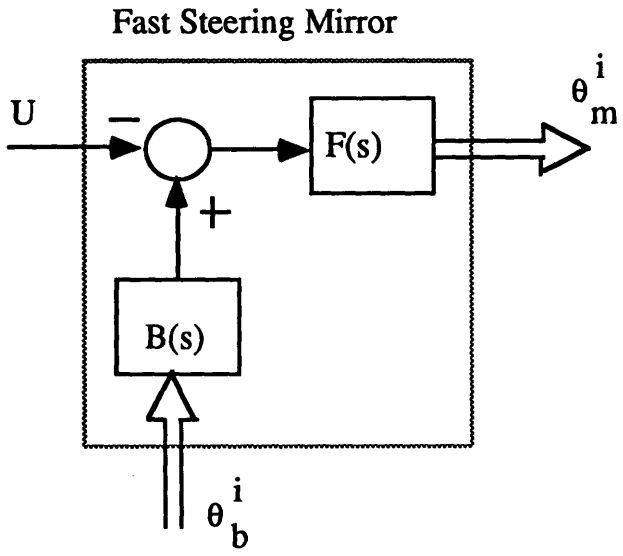

Figure 3.3-2. FSM block diagram.

Figures 3.3-3 and 3.3-4 show the magnitude and phase plots, respectively, after inserting the mirror parameters, of the mirror

control-to-output transfer function, F(s). As can be seen, it is modeled as a simple second-order system with a D.C. gain of 2, poles at 1.5 Hz and a damping factor of 0.056.

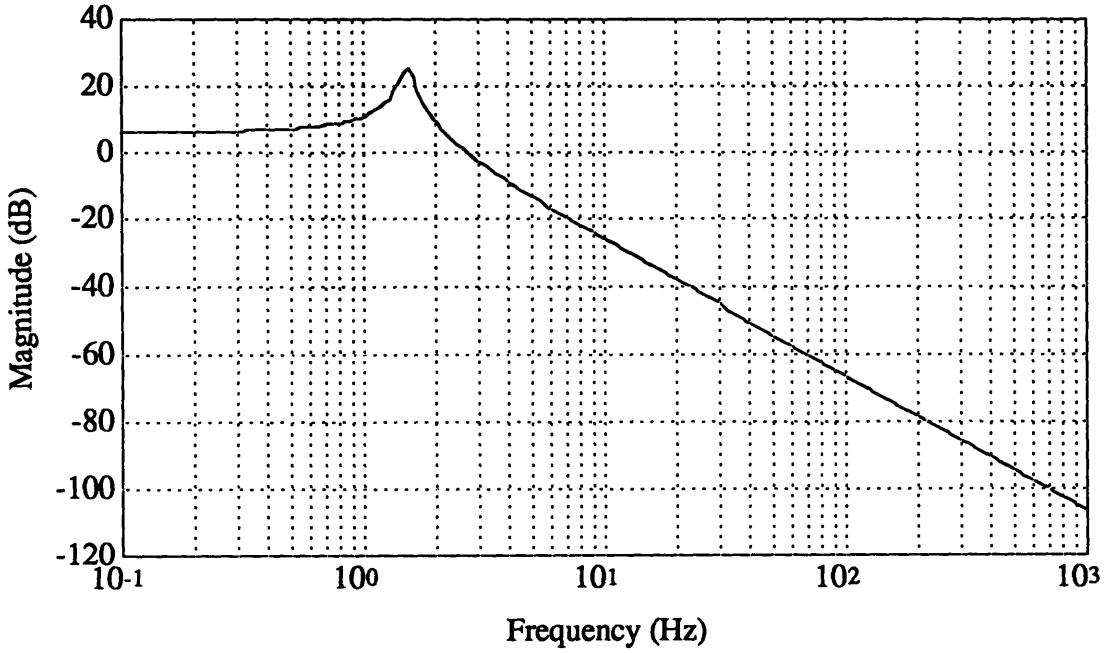

Figure 3.3-3. Magnitude of mirror loop transfer function.

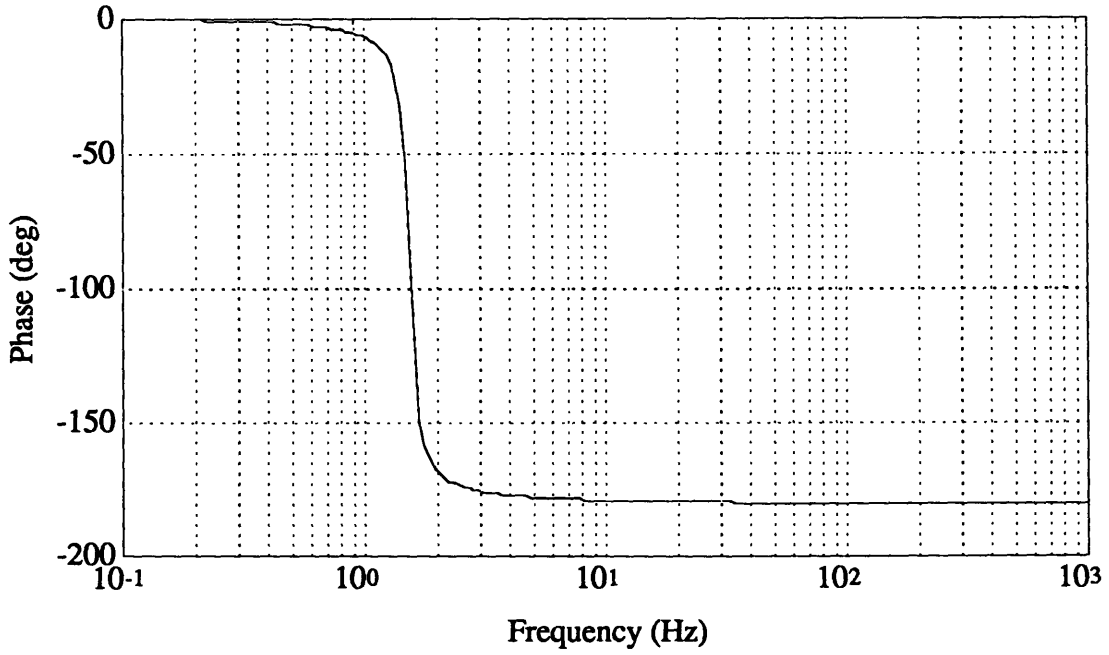

Figure 3.3-4. Phase of mirror loop transfer function.

3.4 Optical Reference Gyroscope

The ORG has fairly complex dynamics due to its gyroscopic and spring properties. Ideally, though, its implementation in the system is such that the ORG reference beam is independent of the base motion and its direction remains inertially fixed. Therefore, the transfer function from the base motion input to the ORG output would be zero and not of particular interest. The ORG dynamics would then only show up as a noise input to the system, identified as θ_r^i. This ideal situation will be the first case analyzed in section 5.4.

In reality, the ORG reference beam axis is not completely independent of base motion. There is actual coupling between the case and rotor possibly due to gas dynamics at low frequencies and/or dynamic spring effects. In addition, there is optical coupling due to relative motion between the light source and the ORG rotor optical axis due to the light source not being mounted on the rotor. These combined effects contribute to a base motion coupling term in the ORG noise.

With this effect included, the ORG noise term can be rewritten as:

$$\theta_{rx}^i = \theta_{rnx}^i + H_1 \theta_{bx}^i + H_2 \theta_{by}^i \qquad (3.4\text{-}1)$$

The subscripts "r" and "b" refer to the reference beam and base motion, respectively. The additional subscripts "x" and "y" are necessary since there is cross-axis coupling present and the "n" subscript on the first term on the right hand side indicates the "ideal" noise term. The on-axis and cross-axis isolation transfer functions are indicated as H_1 and H_2, respectively, and are understood to be functions of the complex variable, s.

The ORG dynamical equations in reference 5 include the effects of disturbance torques on the rotor due to gas dynamics within the ORG. These transfer functions, derived from the reference, are given analytically as:

$$H_1(s) = \frac{\omega_s c_p(\omega_s c_p + Hs)}{(\omega_s c_p + Hs)^2 + (s^2 I + c_d s)^2} \tag{3.4-2}$$

$$H_2(s) = \frac{\omega_s c_p(s^2 I + c_d s)}{(\omega_s c_p + Hs)^2 + (s^2 I + c_d s)^2} \tag{3.4-3}$$

where

ω_s: rotor spin speed
c_p: pressure coefficient for particular gas
H: rotor angular momentum
I: rotor inertia
c_d: rotor drag coefficient

Figure 3.4-1 shows the magnitudes of the two coupling transfer functions for the ORG evacuated to a pressure of 7 μm of Hg. The on-axis plot indicates that the rotor follows the case very closely at low frequencies (<1 Hz). This will result in poor disturbance rejection in this regime. This bears closer examination later on.

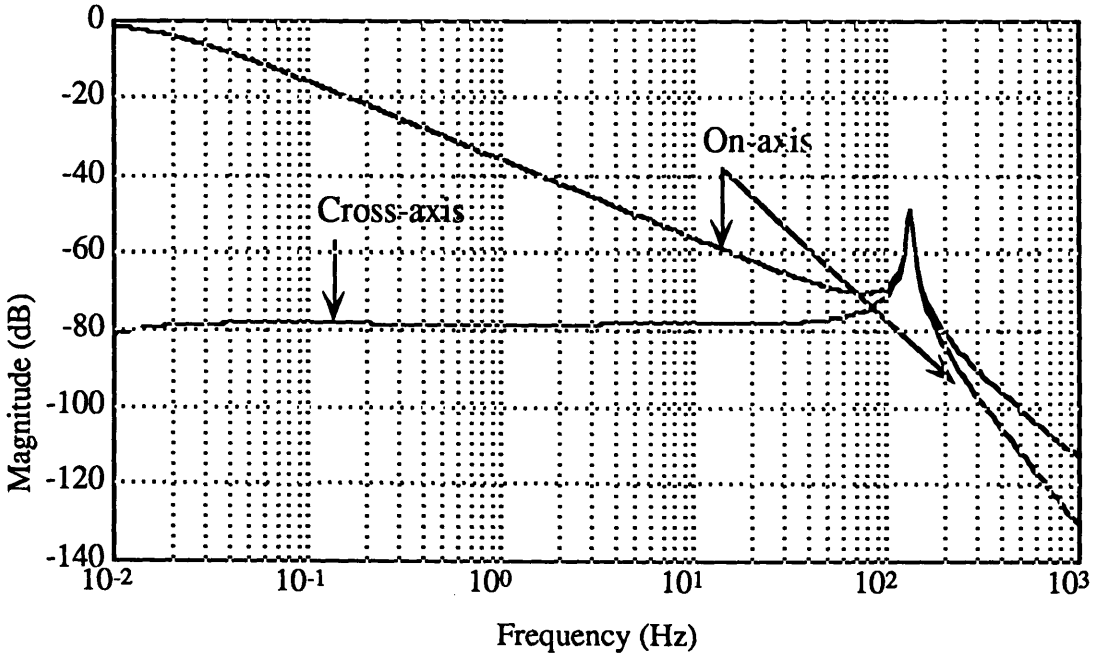

Figure 3.4-1. Magnitude plots of the analytic isolation transfer functions.

As can be seen, the cross-axis isolation term is several orders of magnitude smaller than the on-axis term at low frequencies, and therefore it will be dropped to allow continuing the analysis as two separate loops since the axes appear decoupled. Dropping the cross-axis term and the additional subscripts, equation 3.4-1 becomes:

$$\theta_r^i = \theta_{rn}^i + H_1 \theta_b^i \qquad (3.4\text{-}4)$$

This modified ORG "noise" term will be incorporated into the second analysis case in section 5.4.

3.5 Error Transfer Function Derivations

The system illustrated in figure 1.2-1 can now be represented by the block diagram shown in figure 3.5-1, where the angles are all measured with respect to inertial space as represented by the superscript "i" and the subscripts and other nomenclature are:

b: base motion
m: mirror motion
r: reference beam motion (noise)
t: target motion
e1: image error
e2: detector error

The FSM is represented as shown in figure 3.3-2. The dotted lines are the optical paths, the solid lines are the electrical paths and the broad arrows represent hard mountings. The factor of 2 multiplying the mirror output is the azimuthal multiplier derived in section 3.2 for a mirror rotation about its x axis. The factor is $\sqrt{2}$ for the elevation loop, otherwise the loop structures are identical. The compensator structure, G(s), will be discussed in a later section.

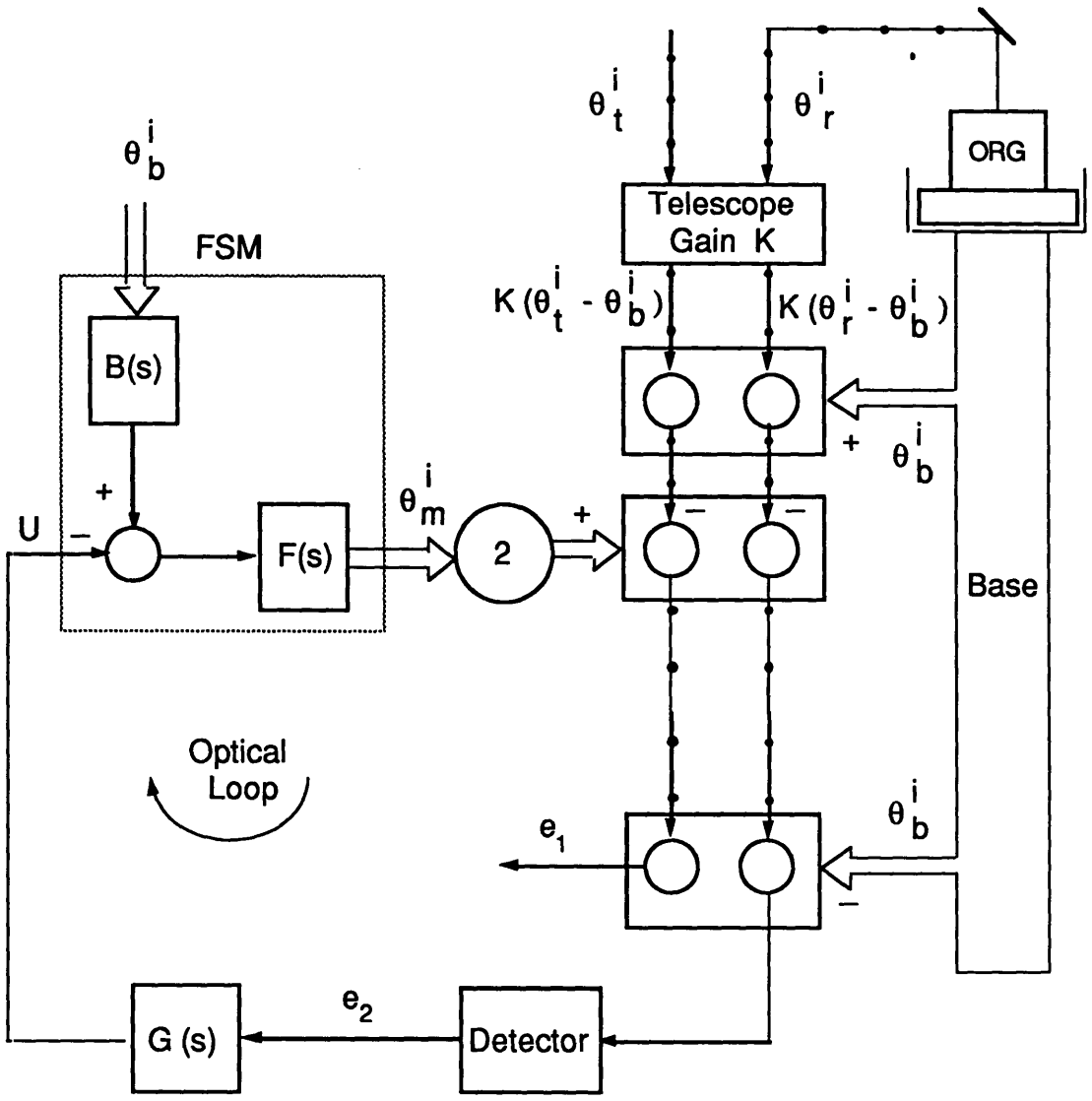

Figure 3.5-1. Image stabilization block diagram.

From figure 3.5-1, the detector error is seen to be:

$$e_2(s,\omega) = 2\,\theta^i_m(s) + (k\text{-}2)\,\theta^i_b(\omega) - k\,\theta^i_r(\omega) \qquad (3.5\text{-}1)$$

where the error, e_2, and the mirror position, θ^i_m, are Laplace transform functions of the complex variable $s = j\omega$. The error is also a function of the real variable, ω, due to the pseudo-random nature of the base motion and the ORG noise.

It is necessary to use the definition from section 3.3 that

$$\theta_m^i(s) = F(s) \left(B(s)\, \theta_b^i(\omega) - U(s) \right) \tag{3.5-2}$$

where the control signal, U, is seen from figure 3.5-1 to be

$$U(s) = G(s)\, e_2. \tag{3.5-3}$$

From this point on, the functional relationships to the variables "s" and "ω" are understood to exist but will be dropped for simplicity.

Using the two relationships above in equation 3.5-1 and solving for the detector error, e_2, gives:

$$e_2 = \left(\frac{(k-2)+2FB}{1+2FG}\right)\theta_b^i - \left(\frac{k}{1+2FG}\right)\theta_r^i \tag{3.5-4}$$

Again, looking at figure 3.5-1, the image error, e_1, can be seen to be:

$$e_1 = 2\,\theta_m^i + (k-2)\,\theta_b^i - k\,\theta_t^i \tag{3.5-5}$$

Inserting the right-hand sides of equalities 3.5-2, 3.5-3, and 3.5-4 into 3.5-5 gives the image error equation:

$$\boxed{e_1 = \left(\frac{(k-2)+2FB}{1+2FG}\right)\theta_b^i + k\left(\frac{2FG}{1+2FG}\right)\theta_r^i - k\,\theta_t^i} \tag{3.5-6}$$

Equation 3.5-6 above is the governing equation for the ensuing analysis as it represents the image error at the focal plane, the term we wish to minimize. Comparing equations 3.5-4 and 3.5-6 we see that

$$e_1 = e_2 + k(\theta_r^i - \theta_t^i) \tag{3.5-7}$$

This shows the common mode subtraction. In the analysis assumptions it was stated that target tracking is not considered so the target motion term will be set equal to zero for the duration.

Notice that the ORG noise enters the detector error equation (3.5-4) as a multiple of the loop sensitivity transfer function (1/(1+2FG)) whereas it enters the image error equation 3.5-6 as a multiple of the closed loop transfer function (2FG/(1+2FG)). Since the detector error is the feedback signal, there will be a residual image error which will require a trade-off between ORG noise rejection and base motion attenuation.

4 Characterization of System Inputs

In order to quantify the imaging error, the base motion disturbance and ORG noise power spectral densities (PSDs) must be identified. This section presents these PSDs and the simplifications made on them to facilitate numerical computations.

4.1 Base Motion Power Spectral Densities

To accurately represent the disturbance spectrum of a spacecraft's input into an optical platform, it is necessary to have fairly detailed design information so that the structural transmissibility and modes can be accurately modeled. Reference 7 provides a good example of a disturbance summary where the design information is specified. It shows the contributions by various system elements in both the time and frequency domains of such components as the momentum wheel assembly, solar array drive and antenna assembly for the Laser Intersatellite Tracking Experiment (LITE) as a payload on NASAs Advanced Communications Technology Satellite (ACTS).

In this experiment there is not a specified platform that can be accurately modeled, therefore two representative PSDs were chosen which attempt to bracket the extremes between very high power densities at low frequencies (< 1 Hz) which drops off very rapidly and a lower power density at low frequencies which persists to higher frequencies and rolls off less rapidly. Figure 4.1-1 shows the two spectra being considered. PSD#1 is from a jitter simulation provided on a candidate platform, where the simulated spectrum, consisting of several discrete noise sources superimposed on a rolling off base, is bounded by straight lines on the log-log scale. The RMS value for this spectrum is 320 μrad over .1-100 Hz. PSD#2 is the best estimate of another candidate platform's spectrum which has an RMS value of 30 μrad over the same bandwidth. These quite different spectra will be used to evaluate the systems disturbance rejection performance.

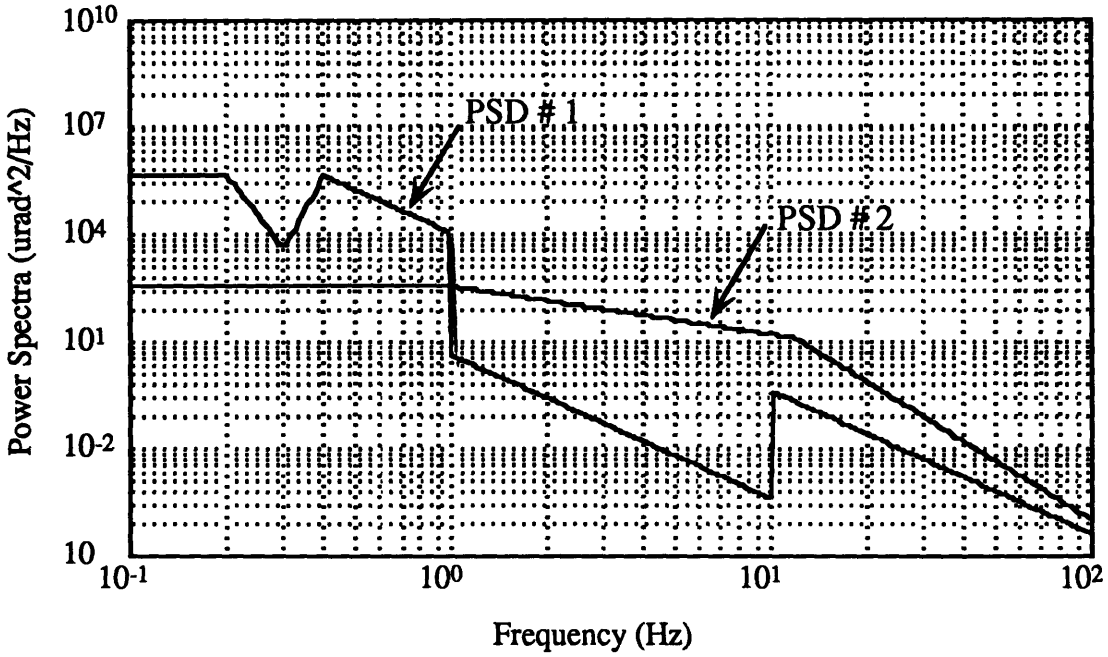

Figure 4.1-1. Base motion power spectra.

4.2 Optical Reference Gyroscope Noise

Figure 4.2-1 shows the test set-up used to measure the ORG noise. Two DYNACs were set up on two reference piers: DYNAC#1 to measure ORG rotor motion and DYNAC#2 (using an internal light source), in conjunction with a mirror mounted on the test table, to measure table motion. The ORG pinhole was illuminated by a helium-neon laser mounted on a third pier. An angular displacement sensor (ADS) with a known scale factor was used to measure table motion very exactly and to calculate a scale factor for DYNAC#2.

Initially, a low bandwidth torque loop was used to make the ORG rotor move with the case and the table was dithered so that a scale factor for the ORG output could be calculated by comparing DYNAC#1 readings with the known factors for the ADS and DYNAC #2 and their associated readings. Once the ORG scale factor was determined, the torque loop was removed, the table was shut down and DYNAC#1 was used to measure the ORG noise PSD.

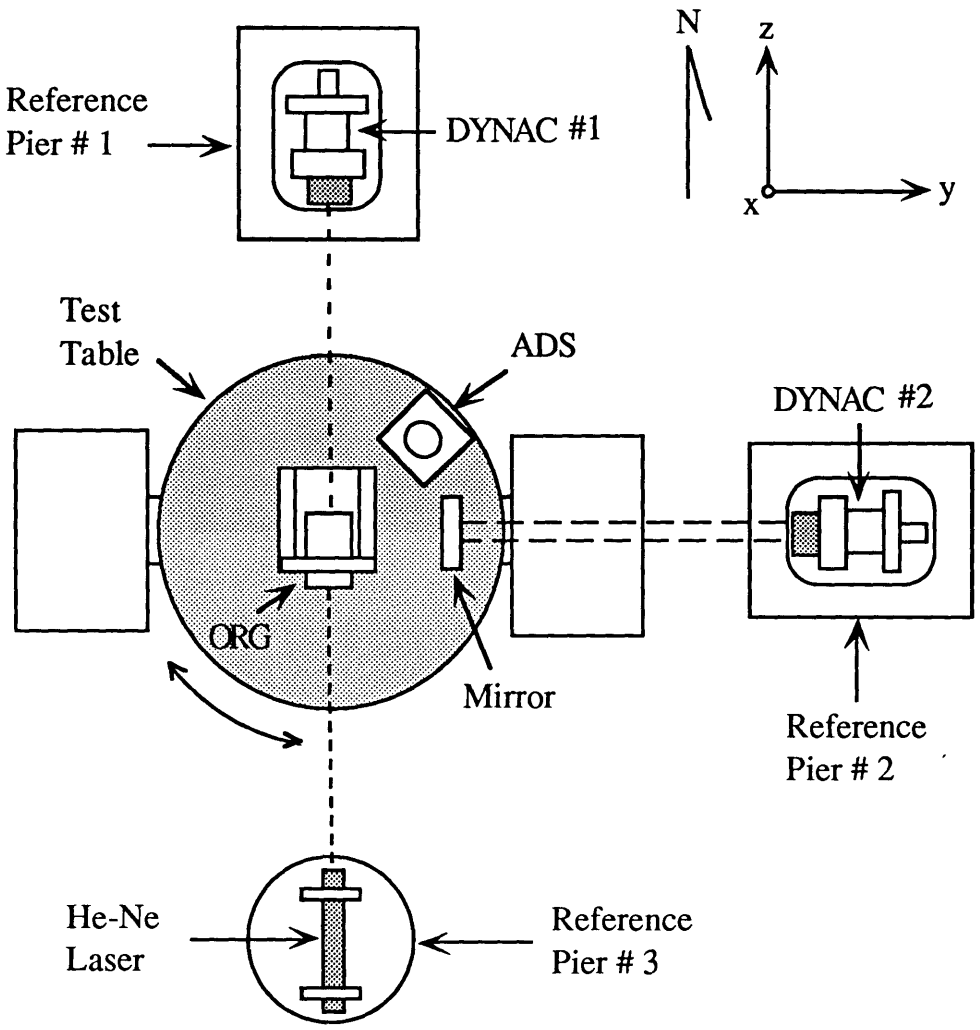

Figure 4.2-1. Test set-up for measuring ORG noise.

Figure 4.2-2 shows the measured noise power spectral density for one of the ORG axes, which is representative of both axes. The wideband noise below 100 Hz is most likely due to light source spatial and temporal variations interacting with the moving pinhole. This interaction is still being investigated. A very large discrete noise source at the spin speed has been suppressed by a very narrow bandwidth phase and amplitude tracking filter called a Subtraction Eliminator [5]. The two large discrete noises at 133 Hz and 180 Hz are the nutation frequency and second harmonic of the ORG spin

speed, respectively. They limit the bandwidth of the system to below the nutation frequency if the performance goals are to be met.

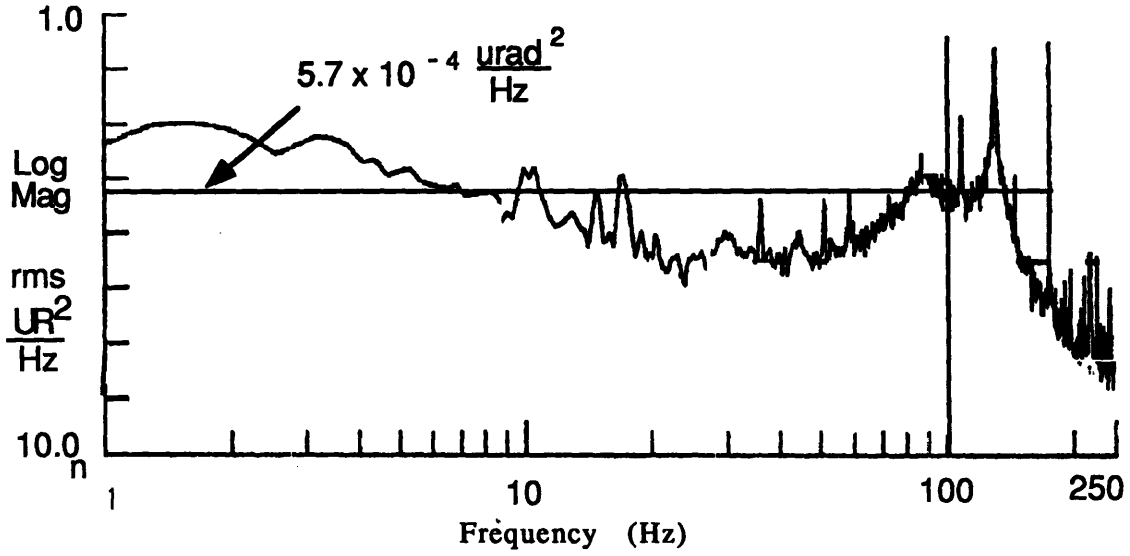

Figure 4.2-2. ORG noise PSD for a single axis.

A possible future redesign of the ORG would raise the spin speed to 200 Hz or greater, moving all the large spin speed related discrete noise out to higher frequencies and allowing for a larger bandwidth. If needed, several of the unique eliminators mentioned previously could be incorporated to eliminate the discrete noises for an even wider bandwidth.

Since the ORG is a prototype device capable of being improved by the techniques mentioned above, little further effort is spent to characterize it here. It can be most simply characterized as a white noise spectrum over the specified bandwidth. The plot shows an integrated power of approximately 57 x 10^{-3} μrad^2 over the 100 Hz bandwidth.

This corresponds to a flat spectrum of

$$\frac{57 \times 10^{-3}\ \mu rad^2}{100\ Hz} = 5.7 \times 10^{-4}\ \mu rad^2/\ Hz$$

which is the ORG noise PSD used in the analysis. It is indicated by the flat line on the plot.

5 Performance Optimization Study

5.1 Compensator Type Selection

Now that the error equations have been derived and the input spectra characterized, an examination of the system performance goals is in order before considering the compensator structure. The following are desired goals:

1. A system bandwidth of .1 -100 Hz is desired. Below .1 Hz, even if the base disturbance was of large amplitude, the effect on image quality would be small since the motion within a short optical integration time is sufficiently small. Above 100 HZ, base motion amplitude is very small since the power required increases as the rate squared, thus the ORG noise becomes the dominant error source.

2. A total RMS image error in the object space of < 1 μrad over the specified bandwidth is desired. The object space is differentiated from the image space in that the beam compressor amplifies angles by the gain, k, thus the computed image error is divided by the same factor to give the error in the object space.

3. As stated in the analysis assumptions previously, tracking is not an analysis topic of this thesis but the system will eventually require tracking while imaging, thus the closed-loop system must provide the tracking capability with zero steady state error for a commanded constant angular rate.

Given the third requirement above, it is necessary to have integral control action for tracking purposes to reduce the steady state error. A consequence of the integral action is that it slows down the transient response. Since spacecraft disturbance spectra have many transient components (such as solar array drive stepping, transition from earth, star, or sun sensors to gyro control when slewing or solar heating driven transients [8]), the transient response must be compensated. The introduction of derivative action in the com-

pensator will provide improved transient response to these disturbance types. Combining proportional control action with the two above gives a resultant, ideal compensator structure of the popular proportional-integral-derivative (PID) type controller so frequently used [9]. It provides the advantages of the three types of control action without their associated disadvantages. This gives a compensator structure in the canonical form:

$$G(s) = \left(k_p + k_d\, s + \frac{k_i}{s}\right) = \frac{1}{s}\left(k_i + k_p\, s + k_d\, s^2\right) \qquad (5.1\text{-}1)$$

This form, though, has a numerator of an order higher than the denominator and will thus add 90 degrees of phase lead in the limit as $s \rightarrow \infty$. The addition of a low pass filter with unity D.C. gain will alleviate this problem and provide an additional roll-off of 20 dB/decade beyond the bandwidth, so we now have a compensator structure of the general form:

$$G(s) = \frac{a}{s(s + a)}\left(k_i + k_p\, s + k_d\, s^2\right) \qquad (5.1\text{-}2)$$

Now it remains to select the values of the four constants in the equation above so that it may be used in the error equations 3.5-4 and 3.5-6 such that the system requirements are satisfied.

5.2 Compensator Parameterization

In order to examine the family of compensators described by equation 5.1-2, a method was necessary to reduce the computational demands required by parametric optimization. We would like to go from $G = G(s, a, k_i, k_p, k_d)$ to $G = G(s, p)$, where p is a parameter that the four constants can be defined by. The parameter selected is referred to as the cut-off frequency, ω_{co}.

The constants are defined in the following manner:

$$a = 3\,\omega_{co}$$
$$k_i = J\,\omega_{co}^3/9 \qquad (5.2\text{-}1)$$
$$k_p = 2/3\ (.7)\ J\,\omega_{co}^2$$
$$k_d = J\,\omega_{co}$$

The constant "J" is the mass moment of inertia of the FSM, whose purpose in the definitions will be explained later. By defining the constants in this manner, the compensator defined in equation 5.1-2 can be written in a factored form as:

$$G(s,\omega_{co}) = \frac{J\,3\omega_{co}^2}{s\,(s + 3\omega_{co})}\left(s^2 + \frac{2}{3}(.7)\,\omega_{co}s + \omega_{co}^2/9\right) \qquad (5.2\text{-}2)$$

In this form, the numerator term in parentheses has the appearance of a second order system in the standard form:

$$s^2 + 2\zeta\,\omega_n\,s + \omega_n^2$$

where

$$\omega_n = \omega_{co}/3 \quad \text{and} \quad \zeta = .7 \quad (\approx \text{critical damping})$$

The other terms consist of a lag filter with a corner frequency of $3\omega_{co}$ and an integrator with a variable gain of $J\omega_{co}$.

Combining this with the FSM transfer function F(s) (equation 3.3-4) gives:

$$F(s)G(s,\omega_{co}) = \frac{P}{(J\,s^2+B_m s+K_{eq})} \cdot \frac{J3\omega_{co}^2(s^2+\frac{2}{3}(.7)\omega_{co}s+\omega_{co}^2/9)}{s\,(s+3\omega_{co})}$$

which can be rewritten as:

$$F(s)G(s,\omega_{co}) = \frac{3P\omega_{co}^2}{s\,(s+3\omega_{co})} \frac{(s^2+\frac{2}{3}(.7)\omega_o s+\omega_{co}^2/9)}{(s^2+\frac{B_m}{J}s+\frac{K_{eq}}{J})} \qquad (5.2\text{-}3)$$

Thus the inertia term, J, cancels out when the mirror dynamics are put in the standard second order form. By changing the single parameter, ω_{co}, the gains for the three types of controller action and the corner frequency for the low pass filter can all be adjusted.

The following brief analysis is provided to give a little insight into the rationale for defining the constants as shown in equation 5.2-1. When the loop transfer function as defined by equation 5.2-3 is evaluated at the value of the parameter ($s=j\omega_{co}$), then

$$FG = \frac{3P\omega_{co}^2}{j\omega_{co}(j\omega_{co}+3\omega_{co})} \frac{((j\omega_{co})^2+\frac{2}{3}(.7)\omega_{co}*j\omega_{co}+\omega_{co}^2/9)}{((j\omega_{co})^2+\frac{B_m}{J}j\omega_{co}+\frac{K_{eq}}{J})}$$

Looking at the mirror dynamics in the denominator second order parenthetical, when $\omega_{co} >> 1$ Hz this term becomes $\approx (j\omega_{co})^2$ since $B_m/J \approx 1$ and $K_{eq}/J \approx 10$. With this approximation, the above becomes

$$FG \approx \frac{3P\omega_{co}^2}{j\omega_{co}(j\omega_{co}+3\omega_{co})} \frac{((j\omega_{co})^2+\frac{2}{3}(.7)\omega_{co}*j\omega_{co}+\omega_{co}^2/9)}{(j\omega_{co})^2}$$

In this form, ω_{co} cancels out of the transfer function and FG becomes

$$FG = \frac{3P(-1+j\frac{1.4}{3}+\frac{1}{9})}{j(j+3)} = \frac{3P(\frac{-8}{9}+j\frac{1.4}{3})}{(3j-1)} = \frac{P(-8+j4.2)}{(9j-3)}$$

With P = 1.04, the magnitude of FG when $s= j\omega_{co}$ is

$$|FG| = 1.04\sqrt{\frac{8^2+4.2^2}{9^2+3^2}} = 1.04\sqrt{\frac{81.64}{90}} \approx 1$$

Thus this technique provides a means of knowing that the crossover frequency of FG is approximately ω_{co}. In this case, however, the loop transfer function is 2FG and it is found empirically that the loop crossover frequency is approximately 1.775 ω_{co}.

5.3 Optimization Process

Having characterized the ORG noise and disturbance inputs, identified the compensator structure and parameterized it, we are now ready to perform the computation of the residual imaging error.

Returning to the image error equation 3.4-6, the value of the telescope gain, k, was chosen to be 4 since that is the value of the beam compressor to be used for the experiment. Although this is not the value to be used on a flight test or an operational system, the image error in the object space is nearly independent of this parameter. Using this gain value and setting the target motion equal to zero gives:

$$e_1 = \frac{2(1+FB)}{(1+2FG)}\theta_b^i + \frac{8FG}{(1+2FG)}\theta \qquad (5.3\text{-}1)$$

$$= T_b\ \theta_b^i + T_r\ \theta_r^i \qquad (5.3\text{-}2)$$

where the transfer functions B, F and G are defined by equations 3.3-5, 3.3-4 and 5.2-2, respectively and T_b and T_r are readily evident by comparing the two equations.

Figures 5.3-1 and 5.3-2 show the magnitude plots of the transfer functions T_b and T_r, respectively, for an arbitrary value of ω_{co} = 50 Hz. The first plot is somewhat typical of a sensitivity transfer function in shape and the second is typical of a closed loop transfer function, as indicated when the error equations were derived.

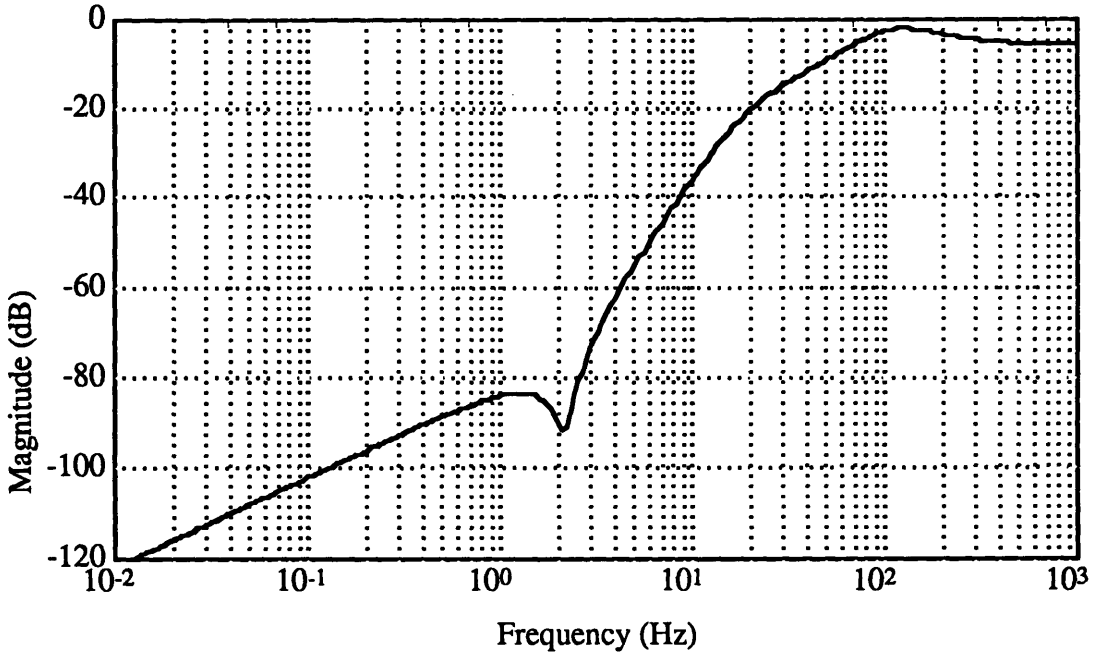

Figure 5.3-1. Magnitude plot of e_1/θ_b^i for a value of ω_{co} = 50 Hz.

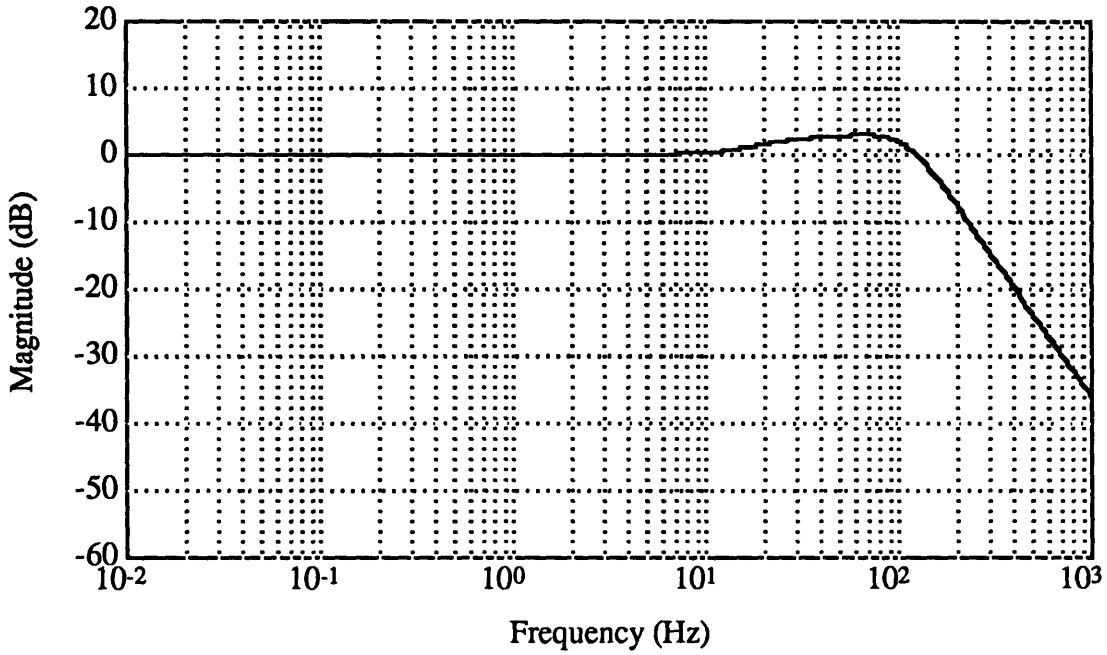

Figure 5.3-2. Magnitude plot of e_1/θ_r^i for a value of ω_{co} = 50 Hz.

Since the base motion and ORG noise are assumed to be independent processes, the RMS image error is calculated using equation 5.3-2 above as:

$$e_{1RMS} = \left(\int_{f_i}^{f_f} \left[|T_b|^2 \, \Theta_b^i + |T_r|^2 \, \Theta_r^i \right] df \right)^{1/2} \qquad (5.3\text{-}3)$$

where Θ_b^i and Θ_r^i are the power spectrum densities of the base motion and ORG, respectively. Since it is not possible to evaluate the integral analytically because the base motion PSDs are not defined by analytic functions and the integrand transfer function forms further complicate the task, equation 5.3-3 must be integrated numerically.

Therefore, equation 5.3-3 is rewritten as a summation in equation 5.3-4:

$$e_{1RMS} = \left(\sum_{m=2}^{n} \left[|T_{bm}|^2 \Theta^{i}_{bm} + |T_{rm}|^2 \Theta^{i}_{rm} \right] \Delta f_m \right)^{1/2} \qquad (5.3\text{-}4)$$

The power densities are given in $\mu rad^2/Hz$ and the transfer functions are evaluated in $s_m = j\,(2\pi f_m)$ where f_m is in Hz. The bandwidth of .1-100 Hz is divided into n-1 logarithmically spaced intervals since the PSDs are specified in a logarithmic domain. The frequency increment is calculated as $\Delta f_m = f_m - f_{m-1}$. To begin the evaluation, the parameter value (ω_{co}) must be specified. Then the RMS error value can be calculated by performing the summation above for each value of ω_{co}.

Since we desire the error in the object space instead of the image space, we must divide the error computed in equation 5.3-4 by the compressor gain factor:

$$e_{1RMS\,(OBJECT)} = \frac{e_{1RMS\,(IMAGE)}}{4} \qquad (5.3\text{-}5)$$

This normalizes the error since both the angle subtended by the target image at the entrance to the beam compressor and all other inputs get amplified by the beam compressor gain factor in the output. This means that the percent shift of the target image angle at the focal plane due to noise sources or disturbances is nearly independent of the gain factor, except for a small portion of the base motion which comes through the mirror dynamics.

5.4 Analytical Results

5.4.1 No Case-To-Rotor Coupling

This section analyzes the ideal situation where the ORG rotor does not follow the case, i.e. no coupling. The analysis was run using the method delineated in the previous section by implementing a computational loop which began with an initial value of ω_{co} = 5 Hz and an increment of 5 Hz up to 100 Hz. Figure 5.4-1 shows the results for both PSDs #1 and #2.

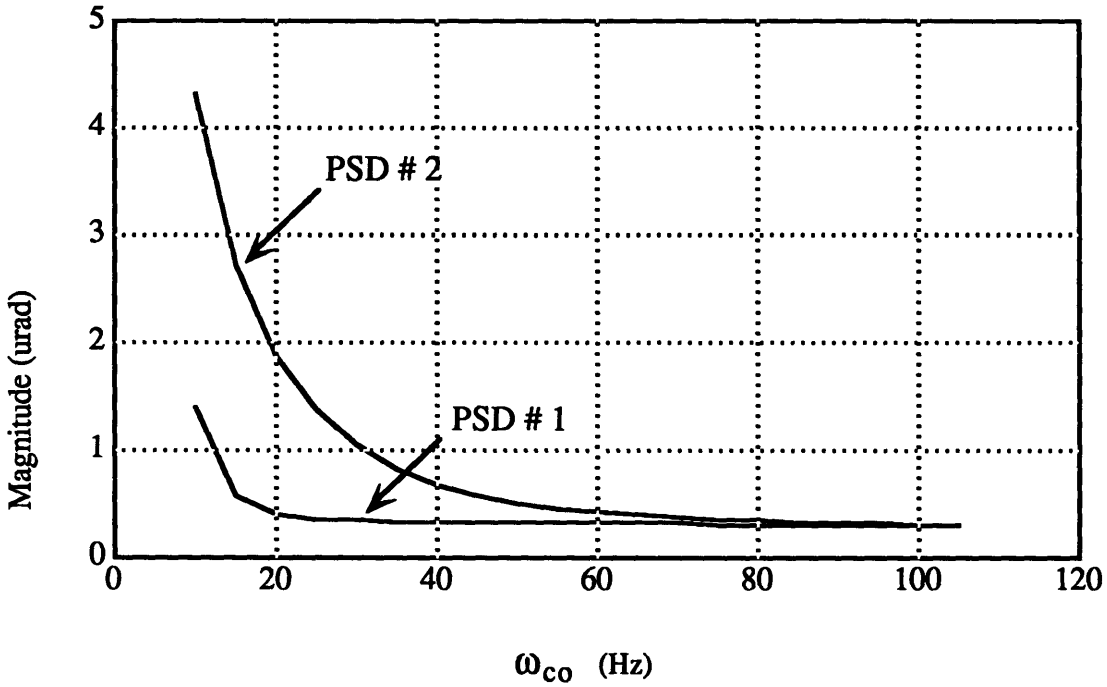

Figure 5.4-1. Residual RMS imaging error versus compensator parameter, ω_{co}, for ideal case-to-rotor isolation.

It shows that the system is able to meet the performance specification for both PSDs with a value of the parameter of about 30 Hz or less. Increasing the parameter increases system bandwidth, providing increasingly better base motion rejection which is most evident in the curve for PSD#2. The curves asymptotically approach the ORG noise value. The point must be made here that the

numerical integration was performed over the specified system bandwidth of .1-100 Hz. Were the integration to continue to a higher frequency, the ORG noise would continue to be integrated and the RMS error value would reach a minimum, then climb slowly.

5.4.2 Analytical Case-to-Rotor Coupling

The previous analysis case assumed perfect isolation between the case and rotor (the ORG was still not perfectly inertial as evidenced by its system noise contribution). This case includes the base motion coupling to the ORG output, which was derived using analytical dynamics in section 3.4. Equation 3.4-4 for the modified ORG noise is substituted into error equations 3.5-4 and 3.5-6. Regrouping of the terms gives the modified error equations:

$$e_1 = \left(\frac{(k-2)+2FB+2kFGH_1}{1+2FG}\right)\theta_b^i + k\left(\frac{2FG}{1+2FG}\right)\theta_r^i - k\,\theta_t^i \qquad (5.4\text{-}1)$$

and

$$e_2 = \left(\frac{(k-2)+2FB-2kFGH_1}{1+2FG}\right)\theta_b^i - \left(\frac{k}{1+2FG}\right)\theta_r^i \qquad (5.4\text{-}2)$$

The result of the coupling is an additional term in the base motion transfer function for both equations. This is the implication of the second general assumption made in section 3.1 that the ORG noise and the base motion were uncorrelated and that any base motion showing up in the ORG noise could be represented in the base motion transfer function. The "n" subscript for the ideal noise in equation 3.4-4 has been dropped since that is again the only component of the ORG noise .

The new base motion-to-error transfer function magnitude plot, T_b, is shown in figure 5.4-2. For frequencies below .1 Hz, there is nearly no disturbance rejection and the best rejection, at any frequency, is just over two decades.

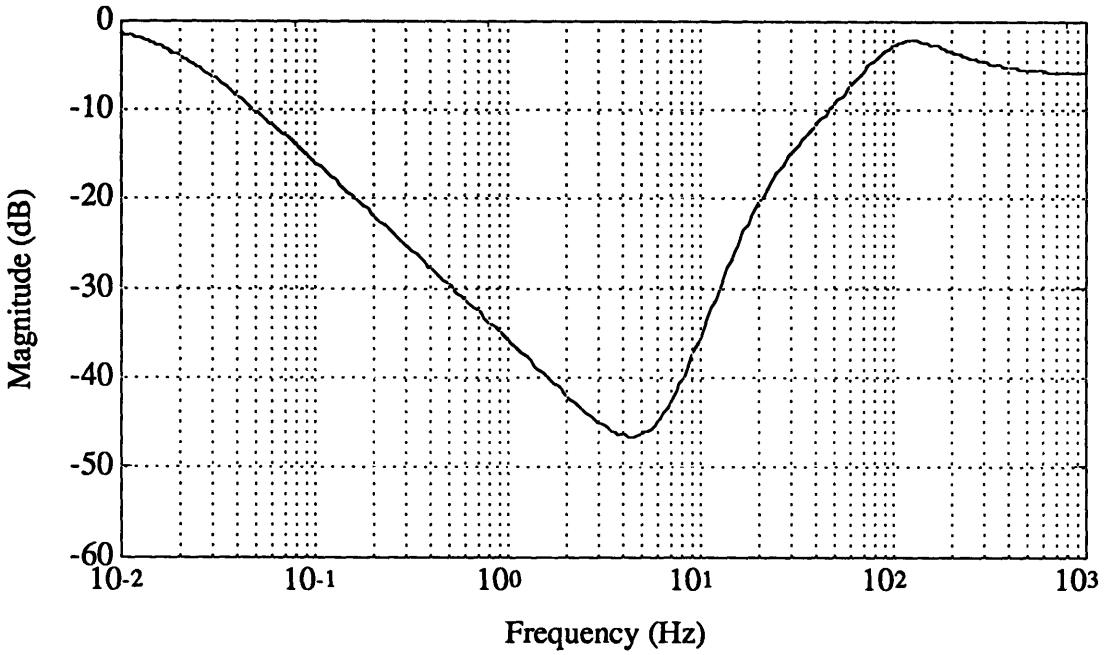

Figure 5.4-2. Magnitude plot of transfer function e_1/θ_b^1 including analytic case-to-rotor coupling.

A simulation was run with the effects of the case-to-rotor coupling present. Figure 5.4-3 shows the results. For both PSDs, the curves are nearly independent of the parameter, except for at very low values of ω_{co}, where the curves come from different directions, reflecting the difference in the distribution of power in the two PSDs. The plot for PSD#1 shows an error of 78 μrad RMS compared to a disturbance spectrum input of 320 μrad RMS. PSD#2 results show much better attenuation with about 2.5 μrad RMS error compared to a 30 μrad RMS disturbance input. Clearly, such results fail to meet any realistic performance goals, thus better case-to-rotor isolation is necessary.

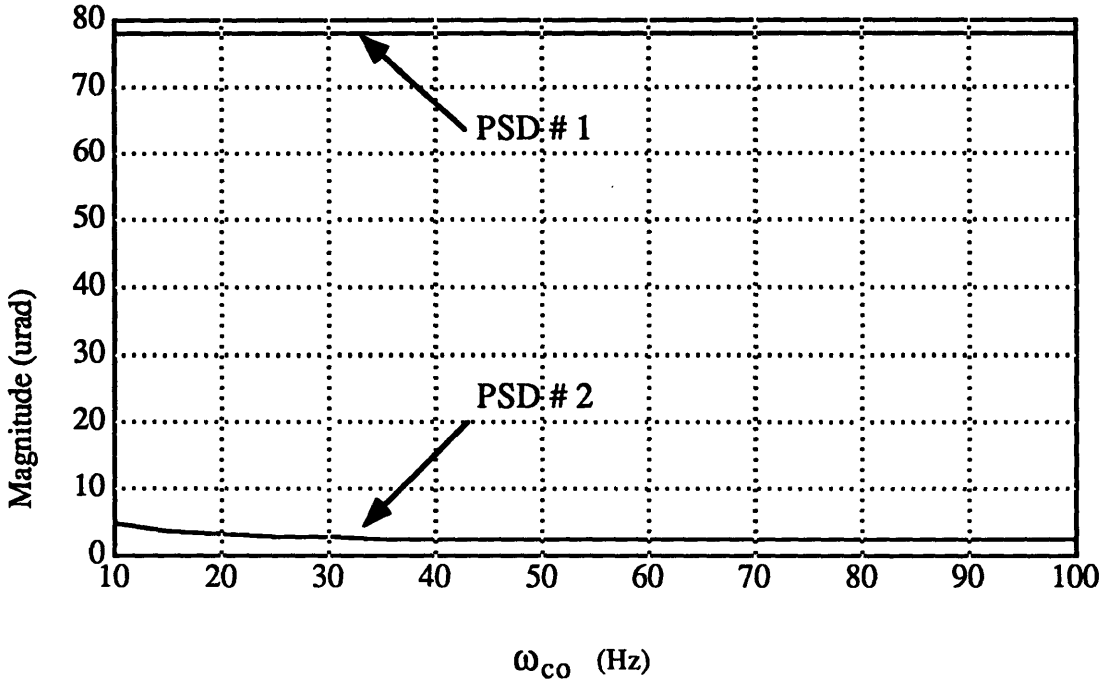

Figure 5.4-3. Residual RMS imaging error, e_1, versus compensator parameter, ω_{co}, with analytical case-to-rotor coupling.

5.4.3 Measured ORG Case-to-Rotor Coupling

The results of the previous section led to a need to better define the ORG case-to-rotor isolation. To this end, an experiment was performed in an attempt to measure the ORG case-to-rotor isolation and invalidate the poor analytical isolation results. Figure 5.4-4 shows the test set-up, where the ORG is mounted on a test table along with a fixed mirror for tracking the table motion. The ORG was evacuated to about 7μm Hg of air to reduce the gas dynamical torques on the rotor.

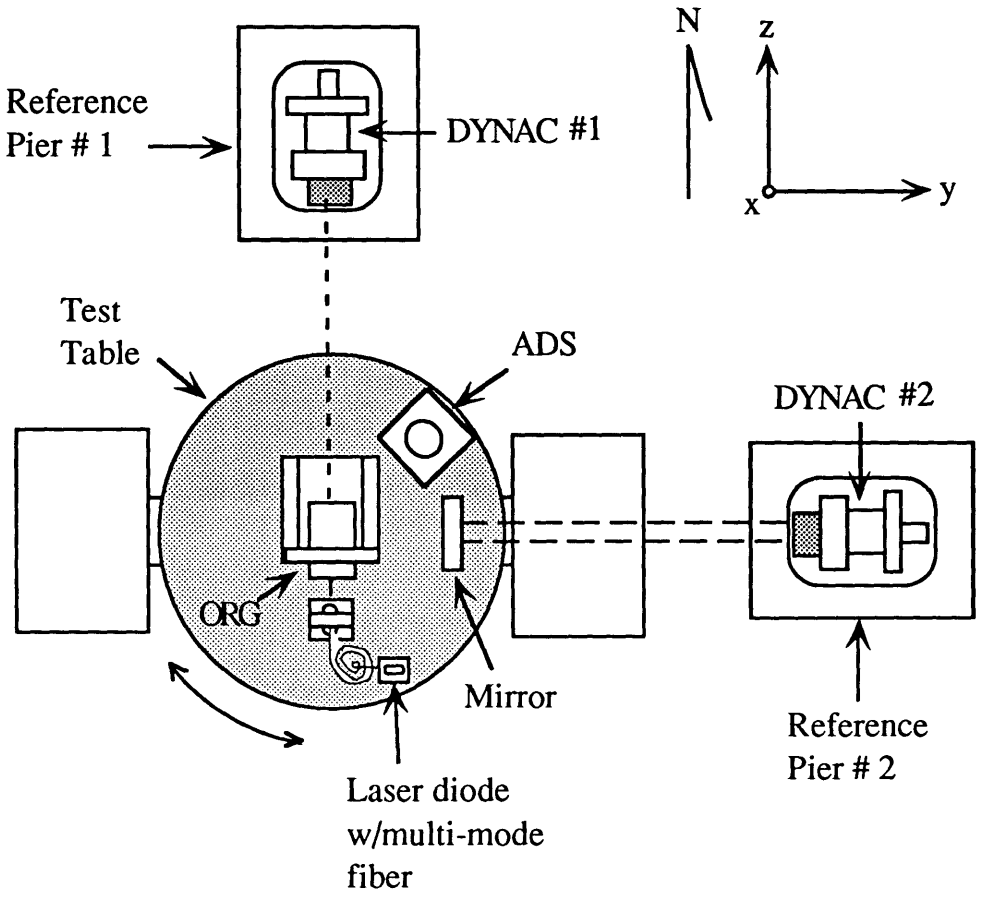

Figure 5.4-4. ORG isolation experiment set-up.

The light source used to illuminate the ORG pinhole was a Spectra Diode laser diode (operated as a light emitting diode) connected to a multi-mode optical fiber. Ideally, the light source would be affixed to the rotor so that no optical deflections between the source and the rotor's optical axis would occur and case mounted optics would be eliminated. A dynamic autocollimator (DYNAC#2) mounted on a reference pier tracked the table motion by emitting its own internal light source which was reflected back from the mirror. Another dynamic autocollimator (DYNAC#1) was mounted on a second reference pier to measure the ORG reference beam when the test table was moved in a swept-sine mode with a peak amplitude of approximately 40 μrad.

Figure 5.4-5 shows the isolation that was measured. It has a value of 10^{-2} μrad/μrad at .1 Hz and rolls off at 1/s till 1 Hz then remains roughly flat at about 10^{-3} μrad/μrad.

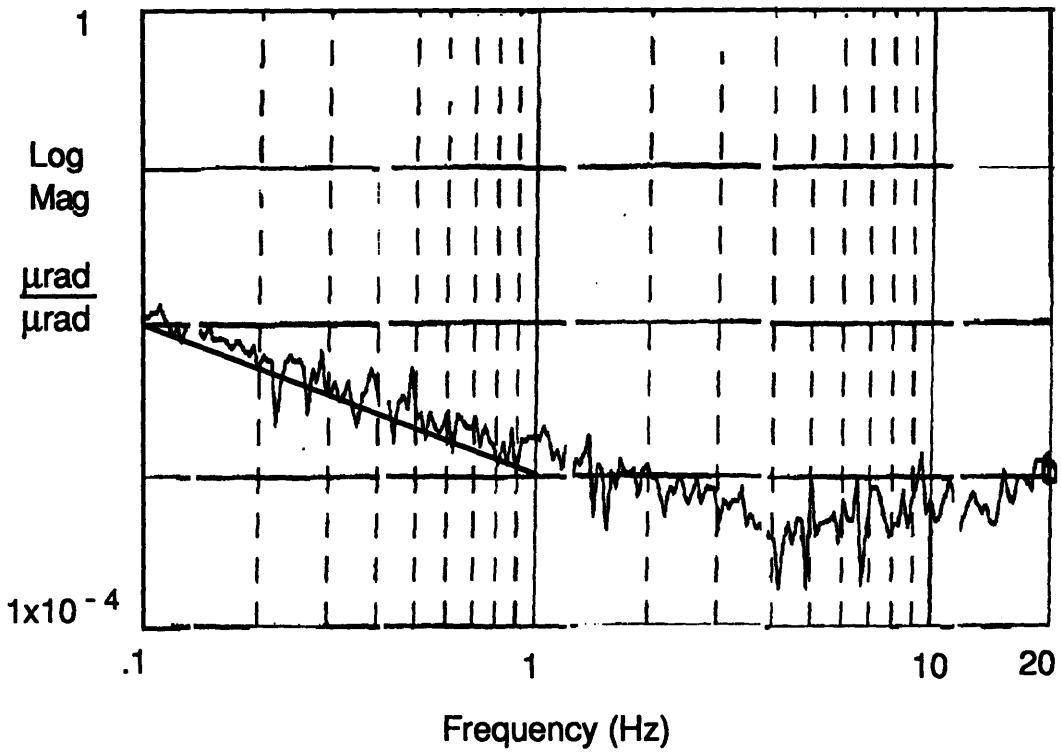

Figure 5.4-5. Measured ORG case-to-rotor isolation.

This approximation to the measured isolation was substituted in for the on-axis isolation transfer function H_1 into error equation 5.4-1 and the new base motion-to-error transfer function is shown in figure 5.4-6. In comparison with the analytical curve of figure 5.4-3, the low frequency portion is now dominated by the improved isolation, while the upper frequency portion of the curve is nearly identical to the previous case.

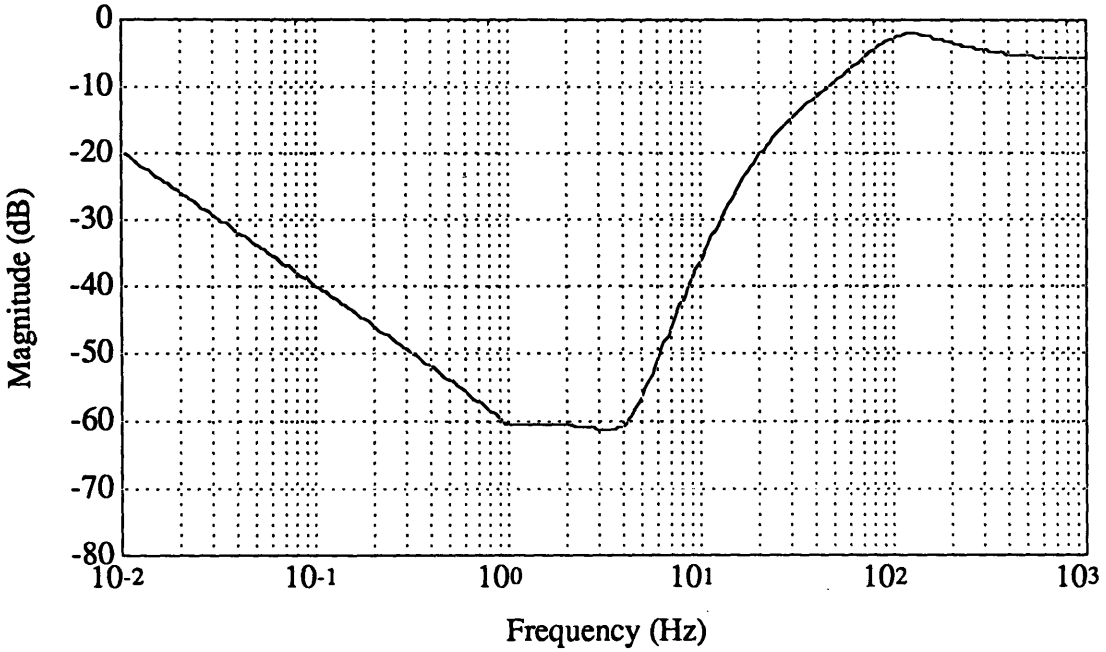

Figure 5.4-6. Magnitude plot of e_1/θ_b^i including measured case-to-rotor coupling.

The analysis was run with this new base motion transfer function and the results are plotted in figure 5.4-7. For PSD #2, we are able to achieve the sub-microradian performance with even a narrow bandwidth (ω_{co} > 31 Hz). In fact, the limiting performance for this type of power spectrum is the asymptotic approach to the ORG RMS noise value of .25 μrad. For PSD #1, however, the best error value achievable for any value of the parameter is about 1.6 μrad RMS due to the very high base motion power below 1 Hz, failing to meet the performance requirement.

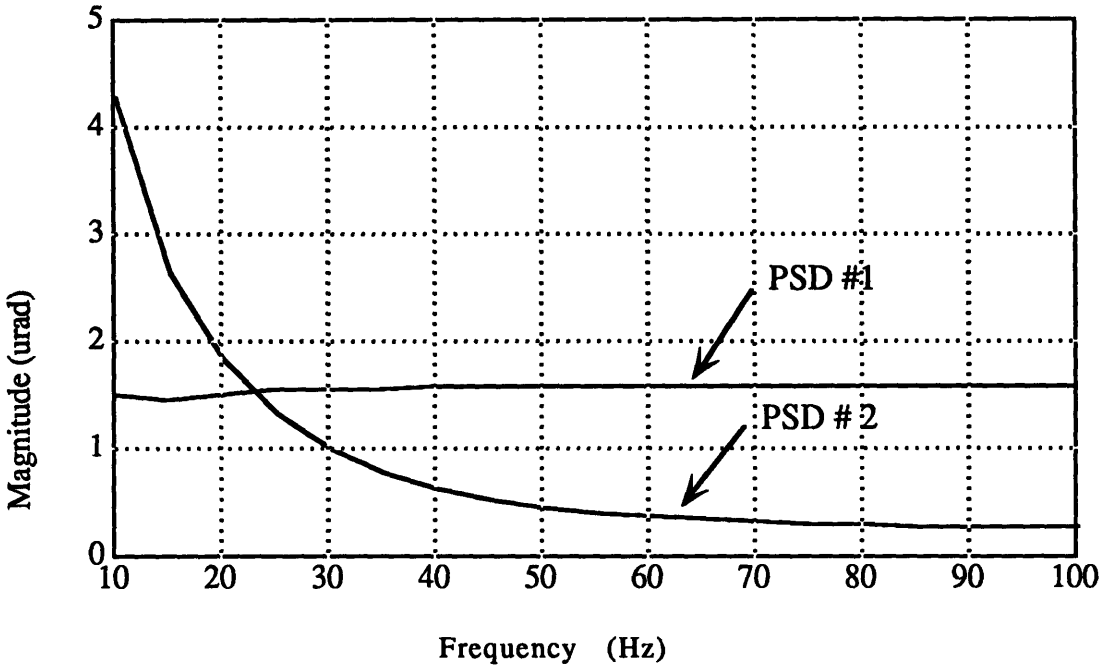

Figure 5.4-7. Residual RMS imaging error, e_1, versus compensator parameter, ω_{co}, for measured case-to-rotor coupling.

5.4.4 Error Weighting Functions

The analysis thus far has not considered the effect of disturbance frequency on image quality and the types of associated image degradation. The image degradation under consideration here is classified as either shift (of the mean) or smear (about the mean). Smear is a phenomenon about which post-processing techniques are ineffective due to its high frequency content and the associated difficulty of capturing the disturbance history for possible subtraction from the sensed image. The shift, however, more readily lends itself to post-processing techniques from information content within the image itself, either in the background or target information, or from external references. Thus, if we can significantly reduce the smear content of the image (that which this stabilization configuration is effective against) and post-processing techniques can eliminate the shift (that which is limited by this

systems isolation) then we can focus our attention on doing the best on the smear and accepting what is achieved on the shift. From this point on, distortion will be used synonymously at times for smear, mainly to differentiate between the subscripts, using "d" for distortion (smear) and "s" for shift.

This section examines the use of weighting functions to split the image error into shift, caused by low frequencies, and smear, associated with high frequencies, with low and high being relative to the integration time. Due to the nature of the PSDs, a statistical analysis using the Fourier spectrum is appropriate. The weighting functions presented below are given here, without proof, from reference 10. The derivations, however, are presented in Appendix A. The method used, very briefly, was to calculate the shift or smear at each point in an image, then to integrate over all frequencies of the disturbance, averaging over all phases in the process.

For mean squared shift, the weighting function is given as:

$$W_S = \frac{2\,(1-\cos C)}{C^2} \tag{5.4-3}$$

where C is defined as

$$C = 2\pi\, f\, \Delta t \tag{5.4-4}$$

with the frequency, f, in Hz and the integration time, Δt, in seconds to give C as an angle in radians. Similarly, the weighting function for the mean squared distortion (smear) is given by:

$$W_d = 2\left[\frac{1}{2} - \frac{(1-\cos C)}{C^2}\right] = 1 - W_S \tag{5.4-5}$$

The factor of 2 in both weighting expressions arises from the fact that the PSDs are normally given in RMS values of disturbance^2/Hz and must be converted to peak amplitudes for integration before taking the RMS values (see Appendix A).

Figure 5.4-8 shows a plot of the two weighting functions as a function of the parameter C. The curves cross at the point $C_1 = 2.78$ or $f_1 = C_1/(2\pi\,\Delta t) = 1/(2.3\,\Delta t)$. Thus, for example, at a value of Δt such as Δt = 1/30th sec, the cross-over frequency is approximately 30/2.3 = 13 Hz. By examination of equations 5.4-3, 5.4-5 and the plots, the functions reach their first local extrema at the value $C=2\pi = 2\pi f\Delta t$, or $f = 1/\Delta t$. This implies that the frequency at which one full cycle is experienced during the integration period may be considered the point at which all frequencies above contribute only to smear and not to shift. Throughout the remainder of this analysis, a value of Δt = 1/30th sec will be used as a worst-case integration time. Any faster integration time will result in less integrated base motion, hence a smaller error.

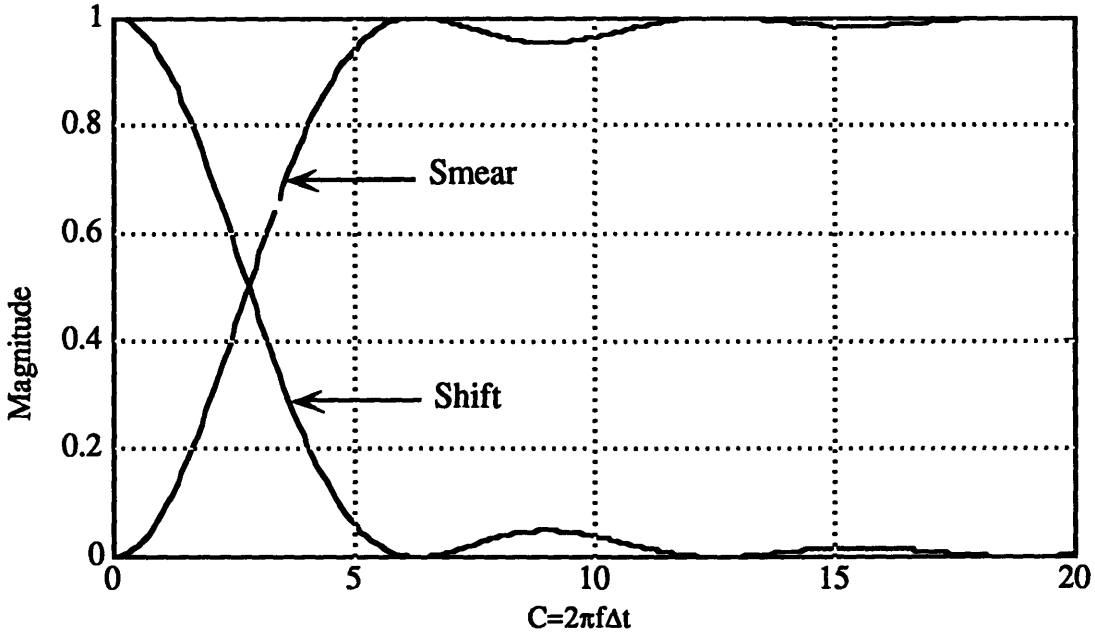

Figure 5.4-8. Weighting function plots.

The weighting functions are applied to the disturbance spectra and integrated over the frequency domain to give the mean squared values of shift and distortion. In this case, the system inputs multiplied by the squared magnitudes of their respective transfer functions which comprise the error spectra may be considered the disturbance spectra, thus the weighting functions are applied directly

to the components of the mean squared error integral, e_1, equation 5.3-3 to give :

$$s_{1RMS} = \left(\int_{f_i}^{f_f} \left[W_s |T_b|^2 \Theta_b^i + W_s |T_r|^2 \Theta_r^i \right] df \right)^{1/2} \quad (5.4\text{-}6)$$

for the RMS shift and

$$d_{1RMS} = \left(\int_{f_i}^{f_f} \left[W_d |T_b|^2 \Theta_b^i + W_d |T_r|^2 \Theta_r^i \right] df \right)^{1/2} \quad (5.4\text{-}7)$$

for the RMS distortion with T_b as defined by equation 5.4-1.

Thus

$$e_{1RMS} = \left(s_{1RMS}^2 + d_{1RMS}^2 \right)^{1/2} \quad (5.4\text{-}8)$$

To examine the impact of weighting on the transfer functions, the square roots of the weighting functions 5.4-3 and 5.4-5 must be applied to the base motion-to-error transfer function so that the base motion contribution to the error is separated into shift and distortion components of the total. Figures 5.4-9 and 5.4-10 show the base motion transfer function weighted as described above. Although the weighting is also applied to the ORG noise, it will not be looked at closely here because the ORG noise is modelled as a flat spectrum and its transfer function is less complex and, therefore, much less illustrative than the base motion portion.

Looking at the shift-weighted function, there is little observable impact on the portion of the curve below 8 Hz as compared to the unweighted case, however above 10 Hz the curve clearly shows the periodic oscillations between zero and a small diminishing amplitude, which rolls off as 1/s. The distortion-weighted plot shows that there is little contribution to distortion by frequencies below 10 Hz.

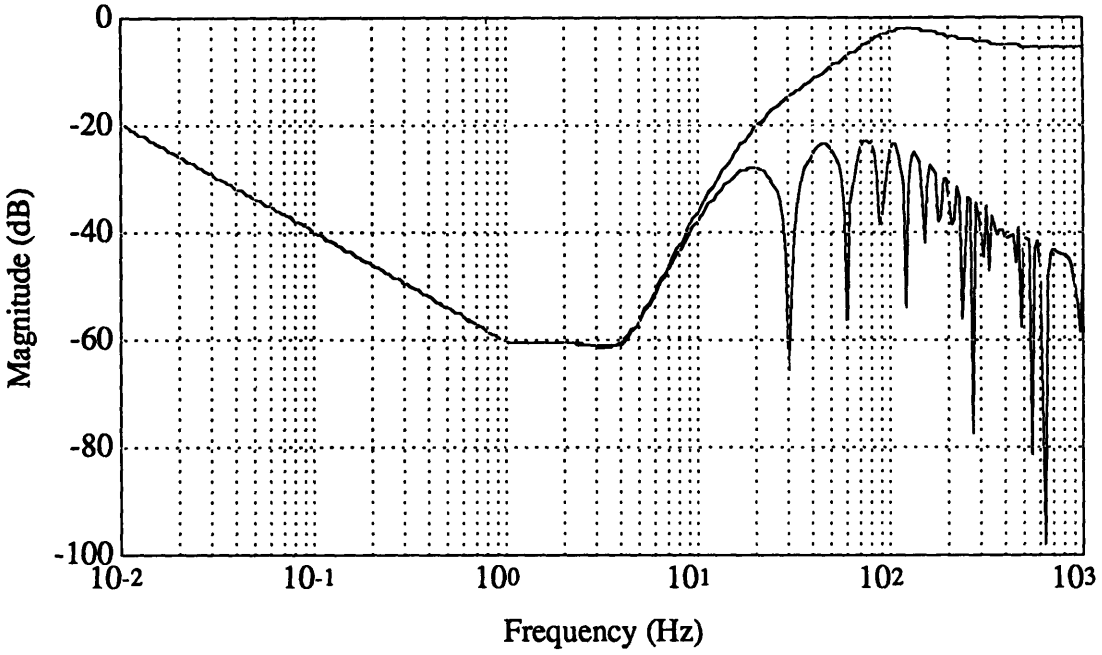

Figure 5.4-9. Magnitude plot of shift-weighted e_1/θ_b^i. The upper curve is the unweighted reference curve.

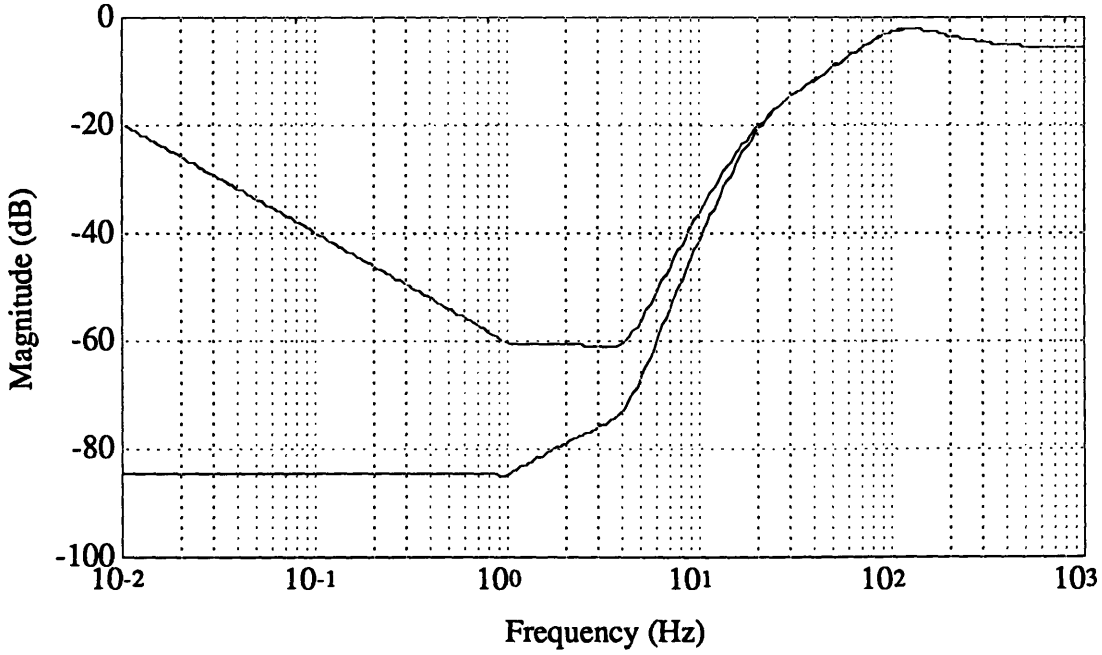

Figure 5.4-10. Magnitude plot of distortion-weighted e_1/θ_b^i. The upper curve is the unweighted reference curve.

The much improved apparent isolation at the low end significantly helps where base motion PSDs have very high power densities at low frequencies.

For computational purposes, the weighting functions are applied in a like manner to the numerical integration equation 5.3-4 and then both the shift and distortion are converted to the object space by dividing by the gain factor. These equations are then reevaluated at each value of the compensator parameter, ω_{co}.

Figures 5.4-11 and 5.4-12 show the analytical results of the shift and smear portions of the imaging error, respectively, as a function of the compensator parameter.

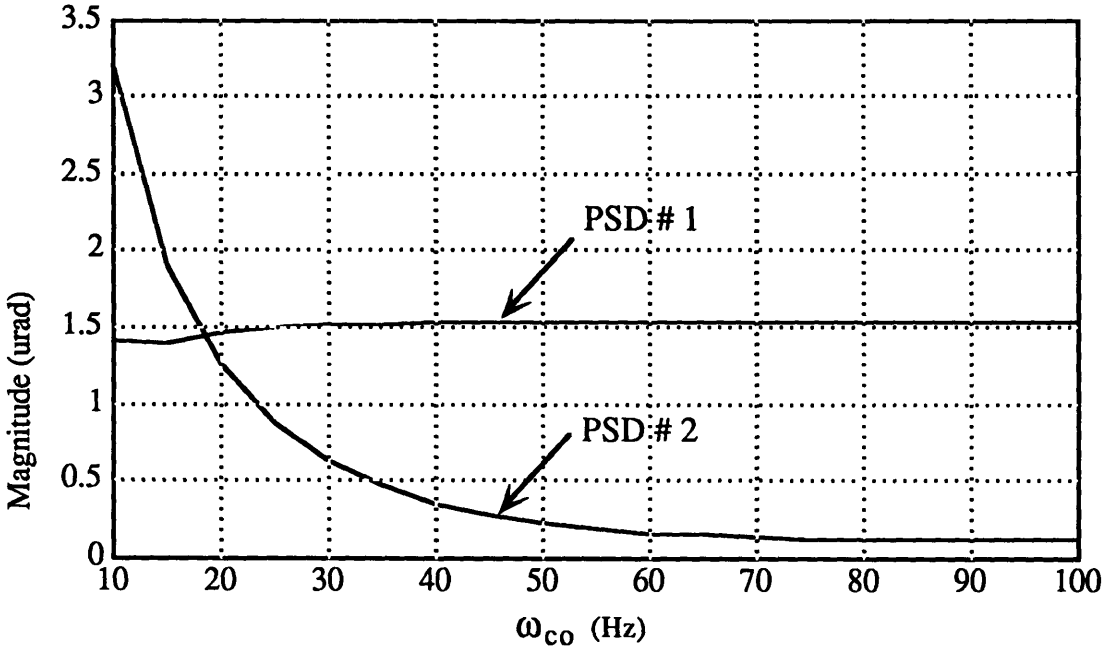

Figure 5.4-11. Shift portion of the residual RMS imaging error, e_1, versus compensator parameter, ω_{co}, for measured case-to-rotor coupling.

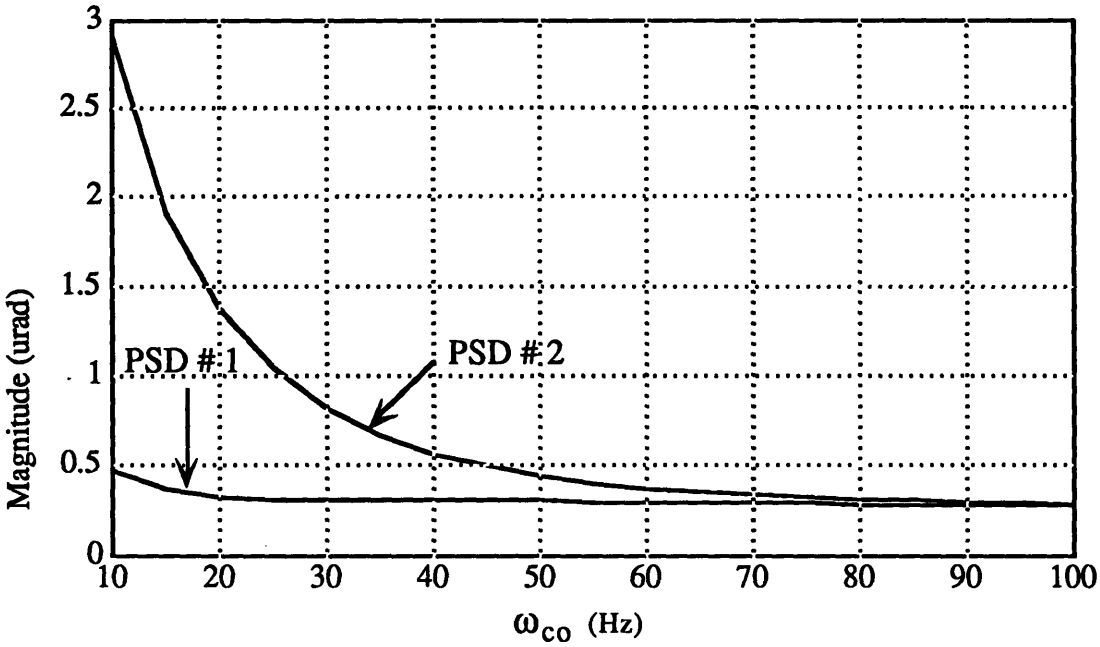

Figure 5.4-12. Distortion portion of the residual RMS imaging error, e_1, versus compensator parameter, ω_{co}, for measured case-to-rotor coupling.

Comparison of the two plots show that for PSD#1, the error is primarily of image shift of approximately 1.5 μrad with only about .3 μrad of image smear. In addition, these values are nearly independent of the parameter, changing little with the parameter except at small parameter values which do not meet the desired bandwidth requirement. These two characteristics reflect the high power densities at low frequencies for this PSD, which rolls off rapidly as seen in figure 4.1-1.

In contrast, PSD#2 results show almost equal values of image shift and smear for all values of the parameter, with the values rolling off rapidly as the system bandwidth increases proportionally with the parameter. At a parameter value of 60 Hz, which gives a system bandwidth of approximately 100 Hz (see end of section 5.2), this PSD contributes to approximately .15 μrad of shift and .4 μrad of smear. This reflects the more uniform distribution of power in PSD#2 as compared to PSD#1.

Both of the smear-weighted curves of figure 5.4-12 approach the ORG noise value of approximately .25 μrad as the parameter continues to increase.

5.5 Summary of Analytical Results

In the previous section four different cases were analyzed parametrically, although the last case was a variation of the third. These case are:

Case 1: Perfect ORG case-to-rotor isolation.
Case 2: Analytical case-to-rotor coupling.
Case 3: Measured case-to-rotor coupling.
Case 4: Measured case-to-rotor coupling with weighting.

The results of the ideal (first) case showed that the performance goals of sub-microradian image error were easily achieved for both PSDs with a parameter value of approximately 30 Hz which corresponds to a system bandwidth of around 50 Hz. The limiting performance was the asymptotic approach to the ORG noise value of .25 μrad RMS.

Including the analytically derived case-to-rotor coupling term into the error equation resulted in poor disturbance rejection due to the high coupling at low frequencies, with the results being almost independent of the system bandwidth. For PSD#1, the computed error was, at best, approximately 78 μrad RMS with a 320 μrad RMS base motion input over .1-100 Hz: an attenuation factor of roughly 1/4. The results for PSD#2 show an image error of about 2 μrad RMS compared to 30 μrad RMS base motion input, which gives an attenuation factor of about 1/15. The poorer attenuation for PSD#1 is attributed to its higher power densities at low frequencies where the coupling is the greatest.

Incorporating the experimentally measured coupling transfer function into the error equation 5.4-1 significantly improved performance over the analytical case. A minimum error of approximately 1.6 μrad was calculated for PSD#1 and .25 μrad for PSD#2. The improved performance was due to roughly an order of magnitude decrease in the measured versus the analytically computed coupling.

The final case introduced weighting functions which were applied as an intermediate step in the computational process. This basically split the calculated error of the previous case into the two components, shift and smear, which, when root-sum-squared, give the total RMS error of the last case. These results indicated that PSD#1 contributed to about 1.5 μrad of shift and .27 μrad of smear for the best results. PSD #2, at low bandwidths, contributes nearly equally to shift and smear. At higher bandwidths, PSD#2 results showed approximately .15 μrad of shift and .3 μrad of smear.

It is interesting to note that the results of the ideal case shown in figure 5.4-1 and the distortion-weighted error results of figure 5.4-12 are nearly identical. This illustrates an observation that if there were perfect isolation between the case and rotor, then the error would be practically all smear (distortion) since low frequency disturbances would be heavily attenuated. So weighting, in this application, can be viewed as separating the error into an ideal (perfect isolation) component plus a coupling error term.

6 System Testing

At the time of this writing, the hardware system described in section 1.2 has just been assembled and only preliminary data is available. The PID controller analyzed in this thesis has not, as yet, been implemented in the system. The present controller, which is a proportional-integral with lead/lag compensator, however, provides the desired bandwidth of .1-100 Hz. The data presented herein, therefore, is shown only as a validation of the image stabilization system concept and does not necessarily reflect the performance predicted by the preceding analysis or mature system performance.

6.1 Test Set-up

A photograph of the test set-up is shown in figure 6.1-1. All of the major elements are shown except for two DYNACs, which are off the right-hand side of the table at the end of the cardboard tubes. A schematic diagram of the test configuration, seen in figure 6.1-2, shows the signal flow more clearly.

The test configuration differs from the original system configuration (figure 1.2-1) in that the simulated target image and the CCD have been replaced by a collimated infrared light-emitting diode (LED) source with a wavelength of 670 μm (as compared to 830 μm for the ORG light source) and a precision angle detector (DYNAC#3) so that a precise scoring could be obtained. The positions of these two components have also been reversed (i.e. "target" on table versus off table) so that the small amount of the LED light source reflected from the beam splitter would not be deflected into DYNAC#3 but would be dumped in the opposite direction. A beam compressor was not used in this early test because its optical qualities introduced performance degradation and its flexible modes may have further complicated the test results. In the figure, DYNAC#1, using an internal light source, measures the table motion and DYNAC#2 measures the residual image jitter. These outputs are sent to channels 1 and 2, respectively of a spectrum analyzer.

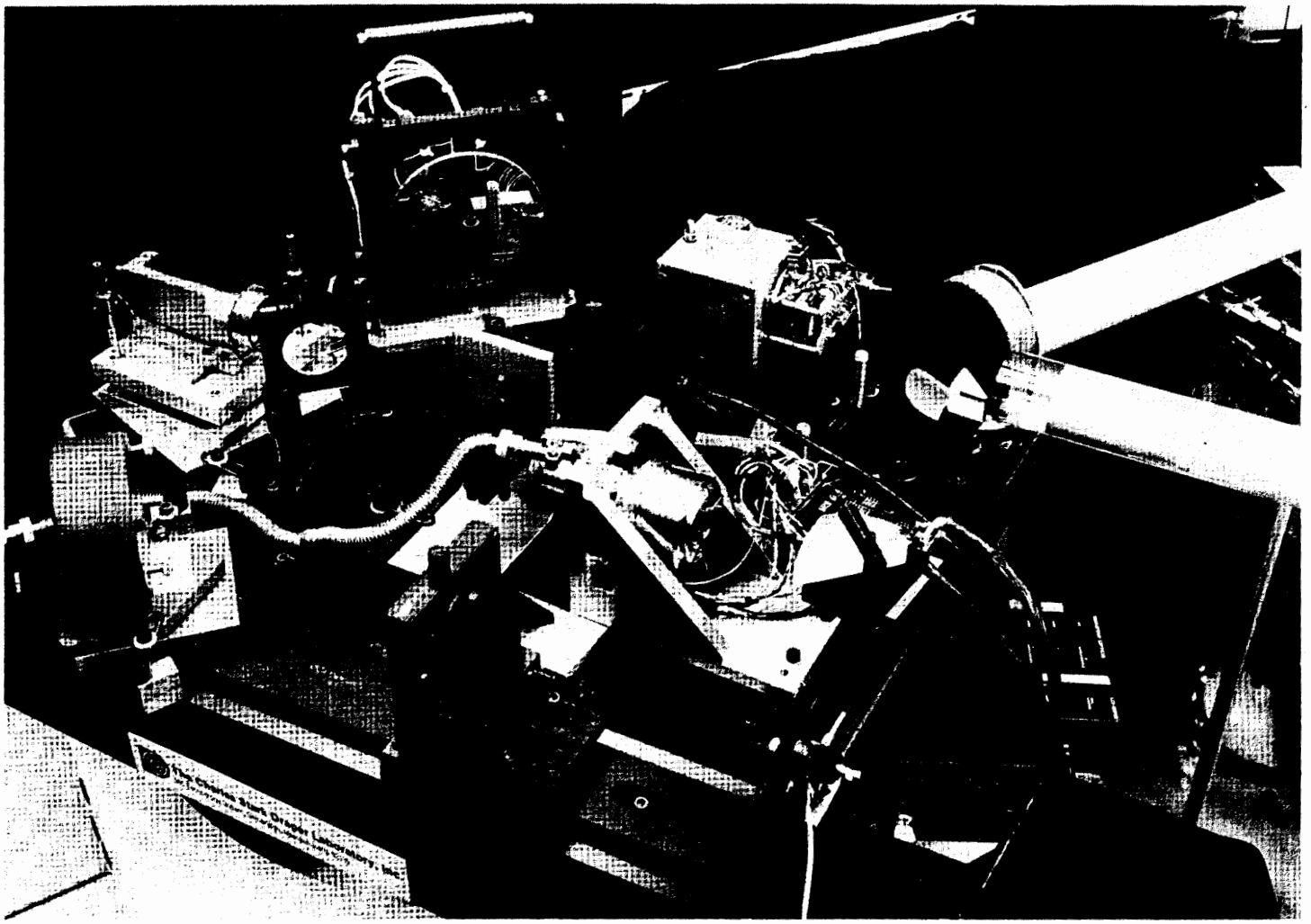

Figure 6.1-1. Photograph of the test set-up.

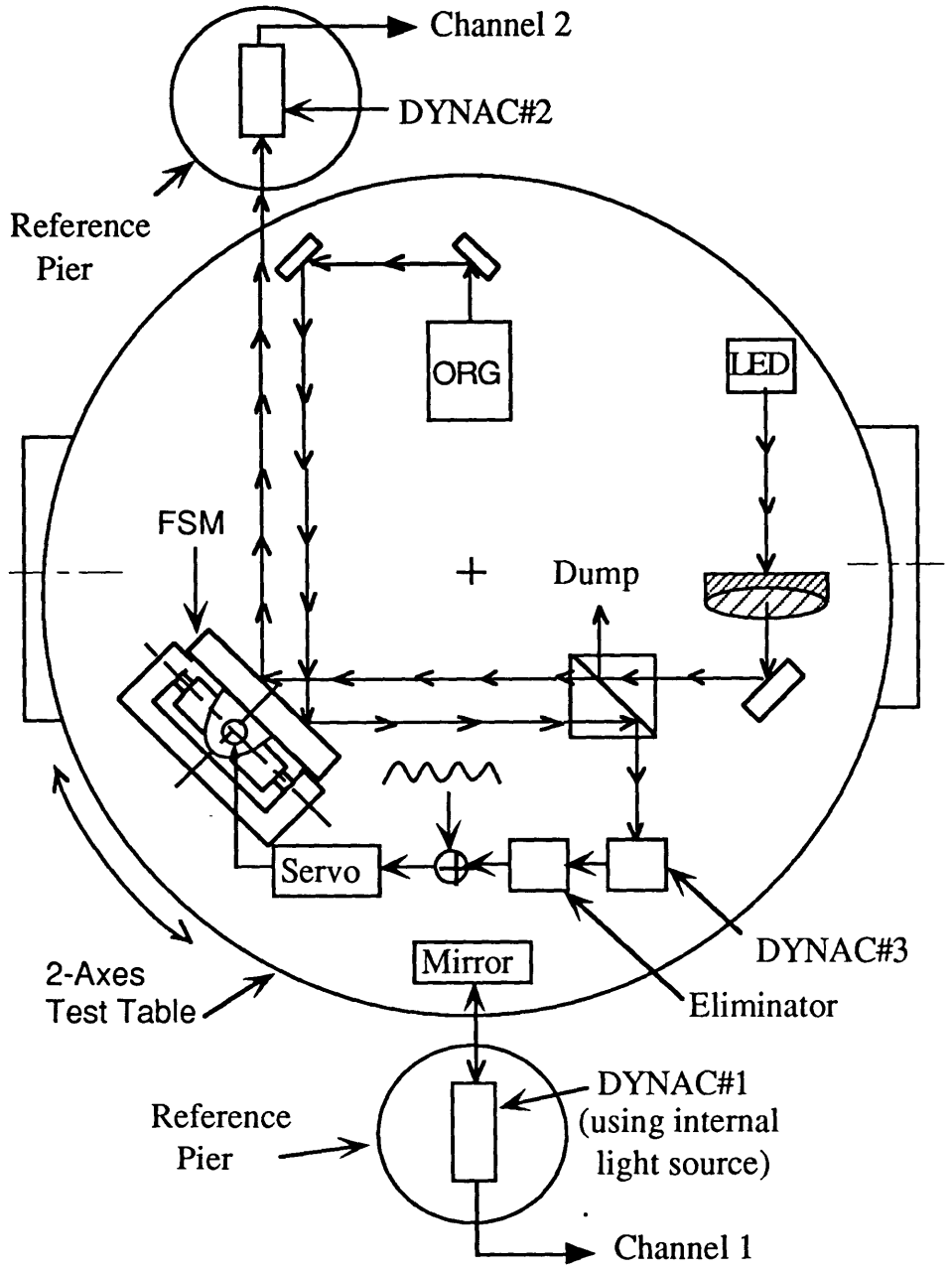

Figure 6.1-2. Schematic of the test set-up.

6.2 Test Results

Preliminary tests were performed to obtain calibrating scale factors for the instruments and to measure test table vibrational noise and inherent noise in the target image path with no base disturbance command to the test table. The test table noise as measured by DYNAC#1 was .15 μrad RMS, .1-20 Hz. Inherent noise in the target image path was measured at 1.92 μrad RMS over the same bandwidth by DNYAC#2. Airflow in the optical path is suspected of being the primary contributor to the latter measurement's high value. Future testing will be performed in a shielded environment. A swept-sine was injected into the closed-loop at the summing junction shown between DYNAC#3 and the servo in figure 6.1-2. The closed-loop transfer function shown in figure 6.2-1 was obtained by measuring the output of Subtraction Eliminator divided by the swept-sine input.

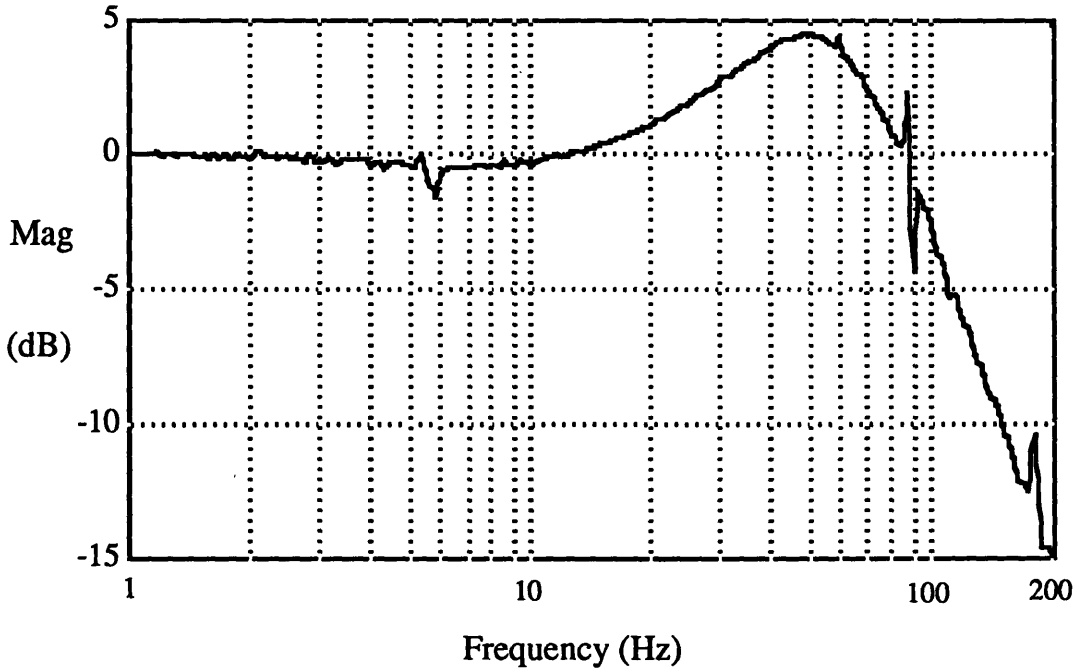

Figure 6.2-1. Measured closed-loop transfer function.

As can be seen, the loop bandwidth is almost exactly 100 Hz, as designed. The anomaly centered at 89.4 Hz is the result of the use of the unique Subtraction Eliminator which greatly attenuates the large

ORG spin speed noise source at the output of DYNAC #3 before sending the error signal to the servo, thus the closed loop does not respond to frequencies in a narrow band around 90 Hz.

The sinusoidal test signal was then removed and applied to the test table torque motor to simulate platform disturbances. This commanded motion was restricted to a bandwidth of .1-20 Hz so as to provide a safe operating margin from the test table's torque-limited acceleration capability yet also provide a sufficient disturbance bandwidth for examination.

Figure 6.2-2 shows the base motion amplitude measured by DYNAC#1. The flat portion of the curve corresponds to a table motion amplitude of approximately 28.7 μrad RMS. The roll-off at the high frequency end is the result of a voltage limit input to the table, thus the table amplitude rolls off as J/s^2 with a constant input torque.

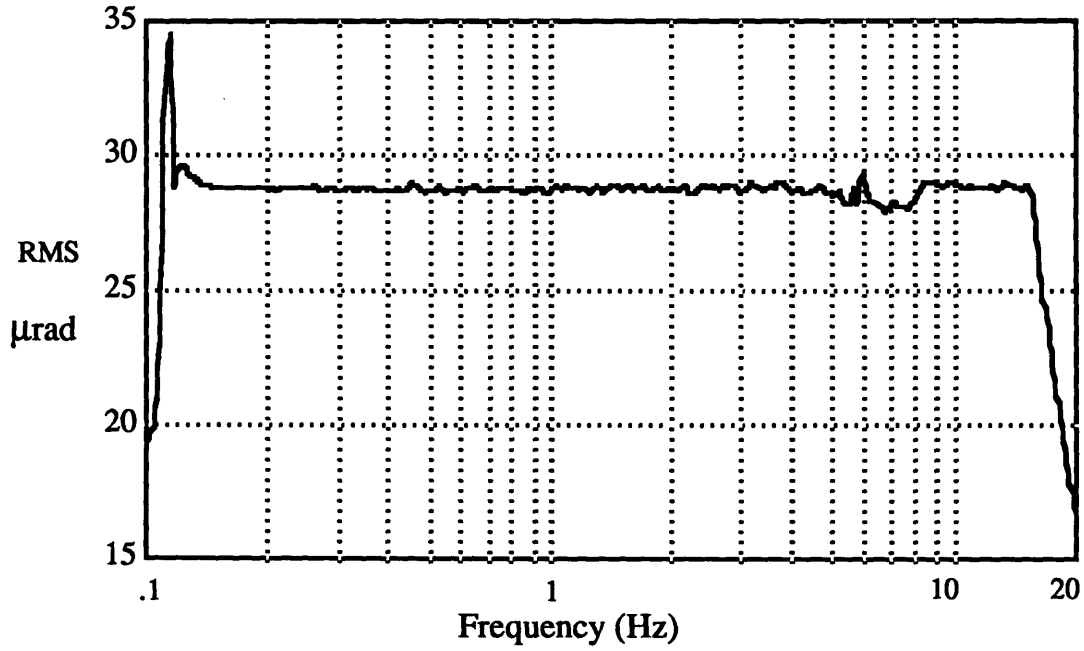

Figure 6.2-2. Measured injected base motion.

The residual pointing jitter, measured by DYNAC#2, is shown in figure 6.2-3. The spike at close to 6 Hz is the result of imperfect spring cancellation in the FSM dynamics. Its presence can also be seen as a small anomaly in the closed-loop transfer function of figure 6.2-1. The mean value of the measured jitter amplitude in the bandwidth below this point is approximately 2.15 μrad RMS.

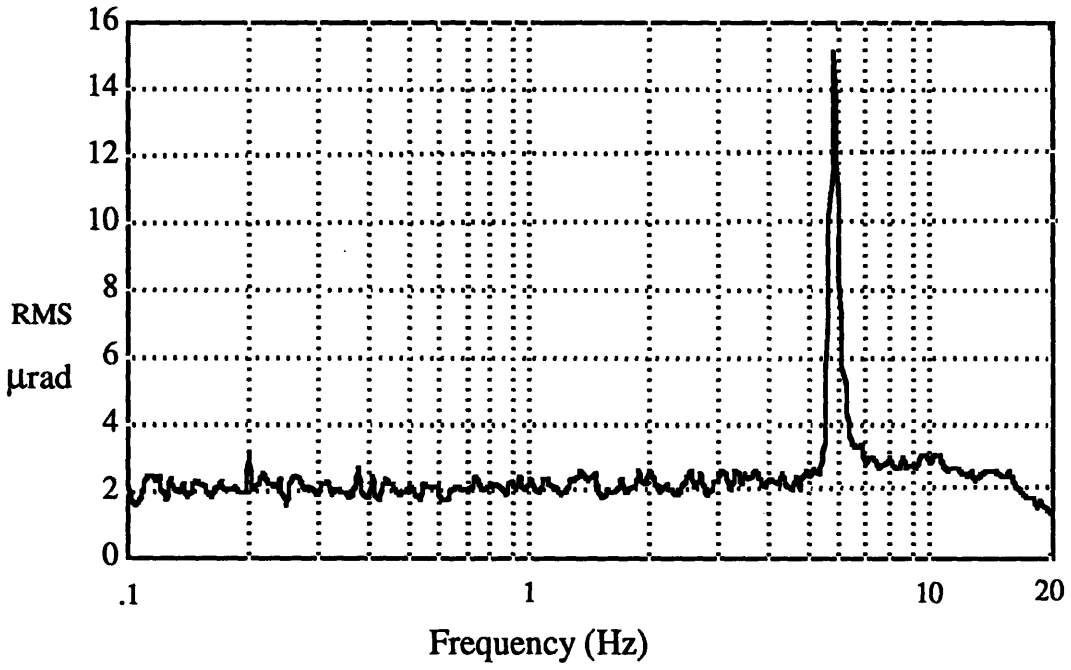

Figure 6.2-3. Measured residual image jitter.

Combining the data from the last two figures as the ratio of the latter over the former gives the isolation transfer function magnitude, which is shown in figure 6.2-4. In addition, the measured phase is shown in figure 6.2-5.

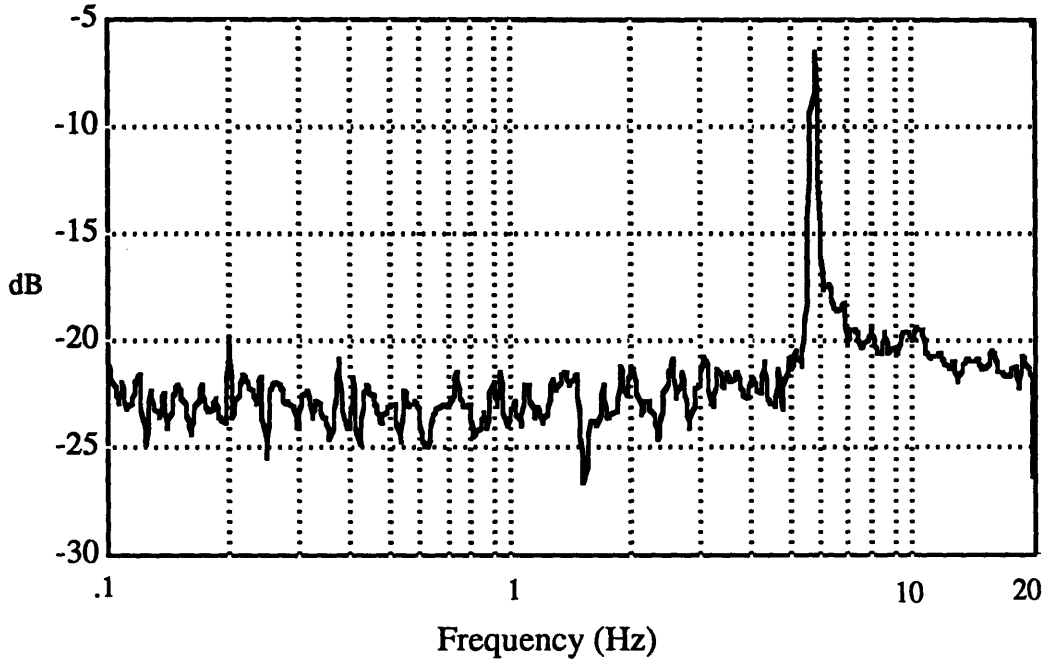

Figure 6.2-4. Measured isolation transfer function magnitude.

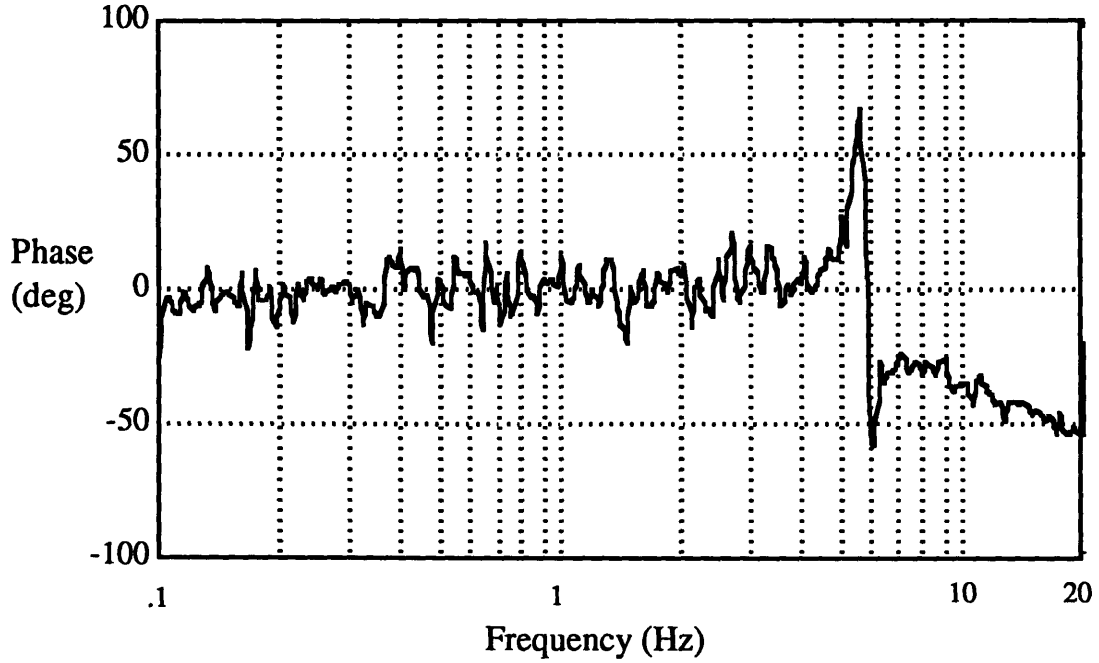

Figure 6.2-5. Measured isolation transfer function phase.

The results shown in figure 6.2-4 show an average attenuation of approximately 23 dB for the bandwidth below the spring effect and the attenuation approaches this value again beyond that point. The phase in the low frequency region has a mean value near zero degrees, as can be seen in figure 6.2-5.

6.3 Comparison of Analytical and Test Results

In comparison with the analytical results, two interesting differences are observed. First, the ORG low bandwidth coupling with a 1/s slope below 2 Hz was not evident. This is probably due to the high evacuation provided in the current test. As a result, the coupling effect is shifted to a lower bandwidth less than .1 Hz so the characteristic 1/s slope does not appear in the measured transfer function. Second, the ORG isolation did not exhibit a 40 to 60 dB attenuation as tested earlier. This remains to be further investigated. Besides these two incompatible observations, the test measurements exactly validate the analytical results. As analyzed in section 5.4.2, the coupled ORG base motion can be considered as an additional noise superimposed on the ORG sensor noise. The coupled ORG base motion, therefore, is fed back to the FSM closed-loop (at 100 Hz) the same as sensor noise or a command input. Therefore, the measured isolation transfer function over .1-20 Hz shows the same response as the FSM closed-loop transfer function except with an attenuated isolation factor contributed by the ORG.

7 Conclusions and Recommendations

7.1 Conclusions

Considering the results of the last two analysis cases, it is possible (analytically at least) with this unique closed-loop system to achieve sub-microradian imaging error performance with a 100 Hz system bandwidth using a PID controller for any reasonable disturbance spectrum. For disturbance power spectra which have very high power densities at low frequencies, sub-microradian performance can be achieved on the distortion but post-processing techniques may be required to eliminate image shift for optimal image quality.

The preliminary tests performed demonstrate the validity of the concept of using the ORG in a closed-loop system for base motion disturbance rejection. In addition, achieving a bandwidth of 100 Hz using the Subtraction Eliminator to attenuate the large ORG spin-speed related noise near 90 Hz was also a significant demonstration. Until the suspected high ORG coupling is corrected, attainment of the desired analytical performance of the system will not be realized.

7.2 Recommendations for Future Research

The following are possible topics of future research associated with the system described herein:

1. Incorporating the structural flex modes of both the platform and the beam compressor on the imaging error would increase the fidelity of the analysis.

2. The additional complication of tracking a moving target and its associated performance evaluation are extensions of this research.

3. The use of the Subtraction Eliminator on the ORG spin speed noise enables the system to have a bandwidth up to its spin rate

frequency. Increasing the spin rate of the ORG will provide larger system bandwidths, resulting in improved disturbance rejection.

8 References

1. Bulloch, C.; *HST-Perfection at a High Price; Interavia Space Markets;* Vol 6, No.2, 1990, pp 59-64.

2. Wintz, P.; Gonzales R.; *Digital Image Processing*, chapters 4-5, pp 140-252, 1997.

3. Herrick, D.; Rodden, J.; Shirley, P.; *End-to-End Control System Verification of the STARLAB Experiment* (AAS 90-45), Vol 72, Advances in the Astronautical Sciences, Guidance and Control 1990., pp 329-342.

4. Swart, G.; Williams, S.; Shattuck, P.; *An Example of On-Orbit Calibration of a Space Based Laser- Zenith Star (AAS 90-043),* Vol 72, Advances in the Astronautical Sciences, Guidance and Control 1990., pp 293-303.

5. Doerr, C.R.; *Optical Reference Gyro Characterization and Performance Enhancement,* Draper Laboratory Report T-1043, MIT Masters Thesis, June 1990.

6. Stecyk, A.; Magee, R.; *DYNAC Interim Design Report,* Draper Laboratory Report CSDL-R-1773, March 1986, 72 pages.

7. Elwell, J.; *Optical Reference Gyro*; United States Patent # 4,270,044; filed April 1979; issued May 1981.

8. Kaufmann, J.E.; Swanson, E.A.; *Laser Intersatellite Transmission Experiment Spatial Acquisition, Tracking, and Pointing System,* MIT/Lincoln Lab Project Report SC-80, September 12, 1989.

9. Takahasi, Y.; Rabins, M.; Auslander, D.; *Control and Dynamic Systems;* Nov, 1972; Section 5-5, pp 187-198.

10. Lucke, R.; *LOS Motion: Jitter & Drift & Distortion & Shift*; Internal Naval Research Laboratory (NRL) paper, Code 6521, 8 pages.

Appendix A

Calculation of Shift and Distortion*

In order to find the LOS motion that results from a sine wave disturbance of amplitude A, frequency f, and phase ϕ, we consider the values of the function $A*\sin(x+\phi)$ over the interval $C=2\pi f\Delta t$:

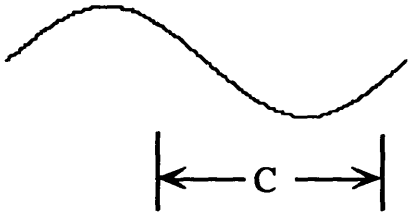

Shift is defined to be the average position over the interval C, i.e., over the picture-taking interval Δt for the frequency f. It is, of course a function of ϕ:

$$s(\phi) = \frac{1}{C}\int_0^C A\sin(x+\phi)\,dx$$

$$= \frac{A}{C}\left(\cos\phi - \cos(C+\phi)\right)$$

Mean square shift, s^2, is found by squaring this expression and averaging over phase $\left(\overline{\{\quad\}}^{\phi}\right.$ means "average $\{\quad\}$ over ϕ "$\left.\right)$

$$s^2 = \overline{\left[\frac{1}{C}\int_0^C A\sin(x+\phi)\,dx\right]^2}^{\phi}$$

---

* This appendix is an excerpt from reference 10. This portion deals only with the shift and smear (distortion) within a single image integration time while the reference also calculates the relative shift and smear between successive images.

$$= A^2 \frac{1-\cos C}{C^2}$$

Similarly, mean square distortion, d^2, can be found by squaring the difference between the actual position and shift, integrating the result over C, and averaging over ϕ (the last two steps are interchangeable - they are both integrations):

$$d^2 = \overline{\frac{1}{C}\int_0^C [A\sin(x+\phi) - s(\phi)]^2 dx}^{\phi}$$

$$= \frac{1}{C}\int_0^C A^2 \overline{\sin^2(x+\phi)}^{\phi} dx - s^2$$

$$= \frac{1}{2} A^2 - s^2$$

$$= A^2\left(\frac{1}{2} - \frac{1-\cos C}{C^2}\right)$$

For a frequency spectrum of RMS disturbance, B, given in units of disturbance/$\sqrt{Hz}$, we note that the amplitude of motion in a narrow frequency band, df, is $A = \sqrt{2}\, B \sqrt{df}$ or $A^2 = 2B^2 df$ (the $\sqrt{2}$ expresses the relation between a sine wave's amplitude, A, and its RMS value, B). Therefore, to find the total rms shift to be expected from this spectrum of disturbance, we must integrate

$$s^2 = A^2 \frac{1-\cos C}{C^2} = 2B^2 \frac{1-\cos C}{C^2} df$$

to get

$$S^2 = \int_0^\infty 2B^2 \frac{1-\cos C}{C^2}\, df$$

The equivalent expression for distortion is

$$D^2 = \int_0^\infty 2B^2 \left(\frac{1}{2} - \frac{1-\cos C}{C^2}\right) df$$

Note that the total mean square position error (shift and distortion) for a discrete frequency disturbance is given by

$$e^2 = \frac{1}{C}\int_0^C \overline{[A\sin(x+\phi)]^2}^{\phi} dx = \frac{1}{2}A^2 ,$$

i.e., just the mean square value of the sine wave, and that $e^2 = s^2 + d^2$. Similarly, from $A^2 = 2B^2 df$, we find, for total mean square position error over all frequencies,

$$E^2 = \int_0^\infty B^2\, df$$

as expected, and $E^2 = S^2 + D^2$, which justified, on a quadrature basis, the separation of LOS pointing error into two components.